

Microscopic description of fission in superheavy nuclei with the parametrization D1M* of the Gogny energy density functional

R. Rodríguez-Guzmán,¹ Y. M. Humadi,¹ and L. M. Robledo^{2,3}

¹ Physics Department, Kuwait University, Kuwait 13060, Kuwait.

²Center for Computational Simulation, Universidad Politécnica de Madrid, Campus de Montegancedo, Boadilla del Monte, 28660-Madrid, Spain

³ Departamento de Física Teórica, Universidad Autónoma de Madrid, 28049-Madrid, Spain

(Dated: April 10, 2020)

The constrained Hartree-Fock-Bogoliubov approximation, based on the recent parametrization D1M* of the Gogny energy density functional, is used to describe fission in 435 superheavy nuclei. The Gogny-D1M* parametrization is benchmarked against available experimental data on inner and second barrier heights, excitation energies of the fission isomers and half-lives in a selected set of Pu, Cm, Cf, Fm, No, Rf, Sg, Hs and Fl nuclei. Results are also compared with those obtained with the Gogny-D1M energy density functional. A detailed study of the minimal energy fission paths is carried out for isotopic chains with atomic numbers $100 \leq Z \leq 126$ including very neutron-rich sectors up to around 4 MeV from the two-neutron driplines. Single-particle energies, ground state deformations, pairing correlations, two-nucleon separation energies and barrier heights are also discussed. In addition to fission paths, the constrained Hartree-Fock-Bogoliubov framework provides collective masses and zero-point quantum rotational and vibrational energies. Those quantities are building blocks within the Wentzel-Kramer-Brillouin formalism employed to evaluate the systematic of the spontaneous fission half-lives t_{sf} . The competition between spontaneous fission and α -decay is studied, through the computation of the α -decay half-lives t_α using a parametrization of the Viola-Seaborg formula. From the comparison with the available experimental data and the results obtained with other theoretical approaches, it is concluded that D1M* represents a reasonable starting point to describe fission in heavy and superheavy nuclei.

PACS numbers: 24.75.+i, 25.85.Ca, 21.60.Jz, 27.90.+b, 21.10.Pc

I. INTRODUCTION.

The theoretical description of fission, one of the many possible decay modes of heavy atomic nuclei [1, 2], still remains one of the hottest topics at the frontier of contemporary nuclear physics. From a semi-classical perspective, fission can be viewed as the result of the competition between the Coulomb repulsion of the nuclear charge density and the nuclear surface energy [3–5]. However, the evolution from the initial configuration (usually the ground state) to the scission point, where the nucleus starts to split into two or more fragments, strongly depends on the intermediate configurations whose properties are deeply influenced by subtle quantum mechanical effects associated with the evolution of shells with deformation, i.e., shell effects. A detailed knowledge of those shell effects is required, for example, to better understand the very limits of the nuclear stability against fission. As one goes up in atomic number Z , Coulomb repulsion among protons overcomes the surface tension and quantum shell effects provide the only mechanism to increase the chances of survival of a given element. Superheavy nuclei belong to the class of nuclear systems where there is no classical fission barrier and, therefore, only quantum shell effects are responsible for their stability. Therefore, they represent the perfect laboratory to understand the subtle quantum effects relevant for the fission dynamics [6, 7] and to obtain key information on the existence of nuclei beyond Oganesson [8].

One of the key applications of nuclear fission concerns the r-process nucleosynthesis of superheavy elements. In scenarios like the dynamical ejecta of neutron star mergers, the competition between rapid neutron captures and beta decays of seed nuclei leads to the synthesis of superheavy elements. The r-process path proceeds to regions of unstable nuclei that undergo fission, recycling the material to lighter products [9–11]. Therefore, fission plays a key role to modify the final shape of the r-process abundances [12, 13] as well as to achieve a robust r-process [14]. Systematic studies of the fission paths and related properties are also very useful to deepen our knowledge of the competition between different decay channels (fission, α -decay, ...) in heavy and superheavy nuclei [15–24]. In addition, nuclear fission remains a topic of high interest for reactor physics, the degradation of radioactive waste, prompt neutron capture data from weapon tests as well as in the context of the synthesis of superheavy elements in laboratories all over around the world [1, 25–30].

From a theoretical point of view, the macroscopic-microscopic (Mac-Mic) model [5, 31–36] has already been successfully applied in systematic studies of superheavy nuclei. Such an approach, provides a very accurate description of the fission landscape in terms of up to five collective degrees of freedom [27, 37, 38]. In recent years the constrained mean-field approximation [39] has emerged as a useful tool for microscopic fission studies [6, 7]. Calculations are typically carried out with non-relativistic Gogny [40–49], Skyrme [50–54],

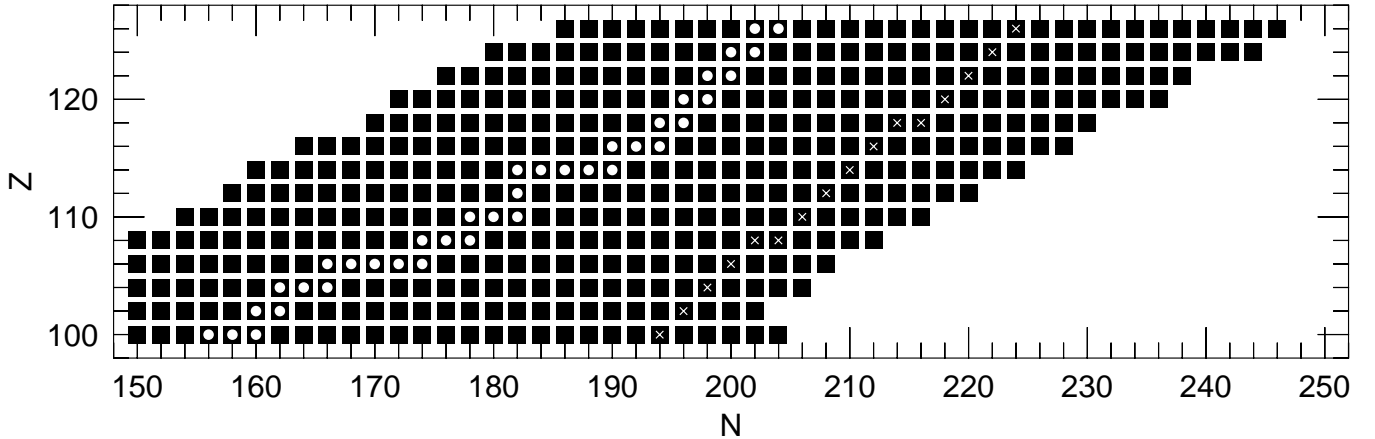


FIG. 1: The black squares represent the set of nuclei considered in this work. The white circles represent the stability line obtained by looking at the minimum of the binding energy as a function of N for constant values of A . The white crosses represent a typical r-process path that is drawn here with the sole purpose of giving an idea of the relevance of the present study for r-process calculations. On the neutron deficient side we reach the proton drip line ($Z > 106$) and in the neutron rich side the frontier corresponds to $S_{2n} \sim 4$ MeV.

and Barcelona-Catania-Paris-Madrid (BCPM) [22, 55] as well as with relativistic [56–62] energy density functionals (EDFs). The (constrained) mean-field approximation provides selfconsistent potential energy surfaces as functions of the quadrupole, octupole, ... deformations. Quantum shell effects are included from the beginning in this unique framework. Moreover, the mean-field approximation also provides in a consistent framework the associated collective inertias as well as the quantum zero-point rotational and vibrational energy corrections. All those are basic ingredients required to compute fission observables like, for example, the spontaneous fission half-lives t_{SF} [6, 7].

The mean-field framework implicitly assumes, that fission properties are determined by general features of the employed EDF. Among the members of the D1 family of parametrizations of the Gogny-EDF, D1S [40] has already built a strong reputation given its ability to reproduce a wealth of low-energy nuclear data all over the nuclear chart both at the mean-field level and beyond [63]. In particular, the Gogny-D1S EDF has already been applied to study heavy and superheavy nuclei [41, 42, 47, 49]. However, one of the deficiencies of the parametrization D1S is the drifting in binding energies along isotopic chains associated to the not so satisfactory neutron matter equation of state (EoS), as compared to more realistic calculations [64]. To cure this deficiency the D1N parametrization [65] was introduced. This parametrization, however, has scarcely been used in the literature [17, 66–69]. On the other hand, the parametrization D1M [70] included in its fitting protocol not only realistic neutron matter EoS information but also the binding energy of all known nuclei. With an impressive rms for binding energies of 0.798 MeV, it represents an excellent and competitive choice to deal with nuclear masses. The suitability of the Gogny-D1M

EDF to describe fission in heavy and superheavy nuclei has been demonstrated in previous studies [17–21] where the results for barrier heights, excitation energies of fission isomers and half-lives have shown a reasonable agreement with the available experimental data as well as with other theoretical studies using different interactions [22, 42, 47, 49]. In addition, D1M essentially retains the same predictive power as D1S in the description of nuclear structure phenomena [66, 67, 71–75].

Unfortunately, the physics of neutron stars (NSs) is not well reproduced by any of the Gogny force parametrizations introduced so far. All the parametrizations turn out to be unable [76–78] to provide NS masses of about two solar masses $2M_{\odot}$, as required by recent astrophysical observations [79, 80]. Moreover, only the Gogny-D1M EDF achieves a NS mass above the canonical value $1.4M_{\odot}$. In order to deal with this problem, a new reparametrization of the Gogny-D1M EDF has been proposed recently. In the new parametrization, denoted D1M* [81], the slope L of the symmetry energy coefficient in nuclear matter is fitted to a value (43.18 MeV) larger than the one in D1M (24.83 MeV) and more according to the expected value for this coefficient. This modification of the parameter L leads to a stiffer EOS for β -stable matter and to NS masses of $2M_{\odot}$. The reparametrization is carried out in a way that all the other relevant combinations of parameters keep their values as to preserve most of the properties of the Gogny-D1M EDF [70, 81]. It has been checked, by means of selected calculations, that D1M* is as good as D1M in describing properties of finite nuclei [82]. However, much more work is still required to assess the performance of D1M*, especially in the case of fission.

The improved value of L leads to the expectation that the nuclear properties of very neutron-rich nuclei obtained with D1M* are going to be more realistic than

TABLE I: The heights of the inner B_I^{th} and second B_{II}^{th} barriers as well as the excitation energies E_{II}^{th} of the fission isomers, predicted with the Gogny-D1M* EDF, are compared with the available experimental values B_I^{exp} , B_{II}^{exp} and E_{II}^{exp} [84, 85]. The B_I^{th} values obtained considering triaxial shapes are given in parenthesis. Results obtained with the Gogny-D1M EDF [17] are included in the table. For each nucleus, the value of Z^2/A is also included in the table to facilitate the comparison of our results with other models/calculations.

Nucleus	Z^2/A	B_I^{th} (D1M)	B_I^{th} (D1M*)	B_I^{exp}	E_{II}^{th} (D1M)	E_{II}^{th} (D1M*)	E_{II}^{exp}	B_{II}^{th} (D1M)	B_{II}^{th} (D1M*)	B_{II}^{exp}
^{234}U	36.17	7.60	7.47	4.80	3.32	2.80	-	8.09	7.72	5.50
		(7.01)	(6.79)							
^{236}U	35.86	8.33	8.34	5.00	3.17	2.67	2.75	8.69	8.07	5.67
		(7.00)	(7.15)							
^{238}U	35.56	9.06	9.14	6.30	3.37	2.82	2.55	9.54	8.97	5.50
		(7.46)	(7.79)							
^{238}Pu	37.13	8.77	8.83	5.60	3.20	2.72	2.40	7.75	7.20	5.10
		(7.66)	(7.80)							
^{240}Pu	36.82	9.45	9.56	6.05	3.36	2.78	2.80	8.57	8.00	5.15
		(7.70)	(7.81)							
^{242}Pu	36.51	9.90	10.08	5.85	3.57	2.90	2.20	9.18	8.66	5.05
		(7.67)	(8.12)							
^{244}Pu	36.21	10.16	10.32	5.70	3.83	3.15	-	9.60	9.03	4.85
		(7.42)	(7.55)			3.15				
^{240}Cm	38.40	8.98	8.91	-	2.55	2.19	2.00	6.13	5.79	-
		(7.87)	(7.83)							
^{242}Cm	38.08	9.78	9.69	6.65	2.77	2.31	1.90	6.99	6.53	5.00
		(8.31)	(8.13)							
^{244}Cm	37.77	10.38	11.02	6.18	3.02	2.47	2.20	7.70	7.15	5.10
		(8.27)	(9.65)							
^{246}Cm	37.46	10.75	10.87	6.00	3.29	2.85	-	8.13	7.89	4.80
		(8.03)	(8.26)							
^{248}Cm	37.16	10.68	9.82	5.80	3.32	2.93	-	8.28	8.00	4.80
		(7.50)	(7.53)							
^{250}Cf	38.42	11.38	10.65	-	2.81	2.58	-	7.09	6.99	3.80
		(8.25)	(7.74)							
^{252}Cf	38.11	10.96	10.39	-	1.37	2.18	-	6.79	6.63	3.50
		(8.07)	(7.27)							

the ones obtained with D1M. As a consequence, D1M* seems to be the appropriate choice to obtain realistic fission properties of very neutron-rich superheavy nuclei as required by astrophysical simulations of nucleosynthesis in the two-neutron start merger scenario. Very neutron-rich superheavy elements live in an unexplored territory where there is an enormous deficit of experimental information and therefore microscopic nuclear structure input is still much required [55, 83]. In this study we use the Hartree-Fock-Bogoliubov (HFB) mean field scheme [39] along with the D1M* parametrization to describe the fission properties of the 435 even-even superheavy systems shown in Fig. 1. The set of nuclei correspond, for each Z value, to roughly 10 nuclei to the left (with respect to the N axis) and 20 to the right with respect to the stability line. This corresponds, in the neutron deficient side to almost the proton drip line. In the neutron rich side we go up to nuclei with $S_{2n} \sim 4\text{MeV}$ covering a wide region of nuclei where the r-process takes place. The suitability of the Gogny-D1M* HFB framework to capture basic fission properties is confirmed by comparing our results for another 22 additional nuclei (see Table I and Fig 2)

with available experimental data [84–87].

The paper is organized as follows. In Sec. II, we briefly outline the theoretical framework used in this study. The results of our calculations are discussed in Sec. III. First, in Sec. III A, we discuss the D1M* results for the nuclei $^{232-238}\text{U}$, $^{238-244}\text{Pu}$, $^{240-248}\text{Cm}$, $^{250,252}\text{Cf}$, $^{250-256}\text{Fm}$, $^{252-256}\text{No}$, $^{256-260}\text{Rf}$, $^{258-262}\text{Sg}$, ^{264}Hs and ^{286}Fl and compare them with available experimental data [84–87] as well as with results obtained with the Gogny-D1M EDF. In Sec. III B, we illustrate the methodology employed to compute the fission paths and other fission-related quantities using the nuclei ^{256}No and ^{298}No as examples. Both sections, are mainly intended to validate the Gogny-D1M* EDF for fission studies. We end Sec. III B, with a brief discussion of the neutron and proton single-particle energies, as functions of the quadrupole moment Q_{20} , in the case of ^{266}Rf which is taken as an illustrative example. The systematic of the fission paths and the fission half-lives obtained for the even-even nuclei shown in Fig. 1 is presented in Sec. III C. In the same section, we also pay attention to the competition between spontaneous fission and α -decay. In ad-

dition, ground state deformations, pairing correlations, two-nucleon separation energies and barrier heights are discussed. Finally, Sec. IV is devoted to the concluding remarks and work perspectives.

II. THEORETICAL FRAMEWORK

In this section, we briefly outline the theoretical framework used in the present study. A detailed account of our methodology can be found in Refs. [17–19]. We have resorted to the HFB approximation with constrains on the axially symmetric quadrupole $\hat{Q}_{20} = z^2 - \frac{1}{2}(x^2 + y^2)$ and octupole $\hat{Q}_{30} = z^3 - \frac{3}{2}z(x^2 + y^2)$ operators [67, 71]. The quadrupole and octupole moments are then computed as $Q_{20} = \langle \hat{Q}_{20} \rangle$ and $Q_{30} = \langle \hat{Q}_{30} \rangle$. The corresponding deformation parameters β_2 and β_3 read

$$\beta_2 = \sqrt{\frac{4\pi}{5}} \frac{Q_{20}}{\langle r^2 \rangle} \quad (1)$$

and

$$\beta_3 = \frac{\sqrt{7\pi}Q_{30}}{3\langle r^3 \rangle} \quad (2)$$

where, $\langle \dots \rangle$ represents the average taken with the corresponding HFB wave function. Aside from these constrains, we include the constrains on both the proton and neutron numbers [39], characteristic of the HFB method. Finally, a constrain on the operator \hat{Q}_{10} is used [67, 71] to prevent spurious effects associated to the center of mass motion that might appear when reflection symmetry (parity) is broken.

The HFB quasiparticle creation and annihilation operators β_μ^\dagger and β_μ have been expanded in an axially symmetric (deformed) harmonic oscillator (HO) basis containing states with J_z quantum numbers up to 31/2 and up to 26 quanta in the z direction. The basis quantum numbers are restricted by the condition $2n_\perp + |m| + \frac{1}{q}n_z \leq M_{z,MAX}$ with $M_{z,MAX} = 17$ and $q = 1.5$. This choice of the parameter q is dictated by the elongated prolate shapes typical of the fission process and is the same used in other similar calculations [17–22, 47]. For each of the studied nuclei and each of the constrained configurations along the corresponding fission paths, the two lengths b_z and b_\perp characterizing the HO basis have been optimized so as to minimize the total HFB energy. The computationally expensive oscillator length optimization along with the large HO basis used guarantees good convergence in the relevant range of shape deformations considered in this work [18, 47].

For the solution of the HFB equations, an approximate second order gradient method [88] has been used. This method guarantees a rapid convergence of the self-consistent HFB procedure as well as an efficient handling of the many constrains imposed. As it is customary in all

the parametrizations of the Gogny-EDF, the two-body kinetic energy correction, including the exchange and pairing channels, has been taken into account in the Ritz-variational procedure. On the other hand, the Coulomb exchange term is considered in the Slater approximation [89] while the Coulomb and spin-orbit contributions to the pairing field have been neglected.

We have computed the spontaneous fission half-life (in seconds) within the Wentzel-Kramer-Brillouin (WKB) formalism [5, 7] as

$$t_{SF} = 2.86 \times 10^{-21} \times (1 + e^{2S}) \quad (3)$$

where the action S along the (minimal energy one-dimensional projected) fission path reads

$$S = \int_a^b dQ_{20} \sqrt{2B(Q_{20})(V(Q_{20}) - (E_{\min} + E_0))} \quad (4)$$

The integration limits a and b correspond to the classical turning points [5] for the energy $E_{\min} + E_0$. The energy E_{\min} corresponds to the ground state minimum for the considered path while E_0 accounts for the ground state's quantal zero point energy associated to the quadrupole collective degree of freedom. In this work, we have performed calculations with two typical values $E_0 = 0.5$ MeV and $E_0 = 1.0$ MeV as it is customary in fission studies [17, 47, 49]. Such an approximation ignores the dependence of E_0 on the softness of the collective potential as well as its dependence on particle number. However, in future more microscopic studies of the E_0 values are needed in order to verify whether this conventional range of 0.5–1.0 MeV is accurate enough.

In Eq. (4), $B(Q_{20})$ represents the collective mass for the quadrupole degree of freedom. The collective potential $V(Q_{20})$ is given by the HFB energy minus the zero-point rotational energy correction $\Delta E_{ROT}(Q_{20}) = \langle \vec{J}^2 \rangle / (2\mathcal{J}_Y)$ and minus the zero point energy associated to the axial quadrupole vibration $\Delta E_{VIB}(Q_{20})$. For the evaluation of the collective mass and the zero-point vibrational energy correction two methods have been used. One is the “perturbative” approximation [91–93] to the Adiabatic Time Dependent HFB (ATDHF) scheme. The second method is based on the Gaussian Overlap Approximation (GOA) to the GCM and also using the “perturbative” approximation. Details on how to compute the required quantities can be found, for instance, in Refs. [7, 17, 25]. The rotational correction $\Delta E_{ROT}(Q_{20})$ has been computed, in terms of the Yoccoz moment of inertia \mathcal{J}_Y , according to the phenomenological prescription discussed in Refs. [94, 95]. In principle, the numerical pre-factor in front of the exponential of the action in Eq. (3) and related to the assault frequency, should be computed taking into account the properties of the ground state minimum. However, this effect amounts at most to a factor of 2 in t_{SF} which is much smaller than the uncertainties in the estimation of the half-life arising from the theoretical uncertainties of the ingredients of the action [17]. Let us also mention that, in the computation of the spontaneous fission half-lives, the wiggles

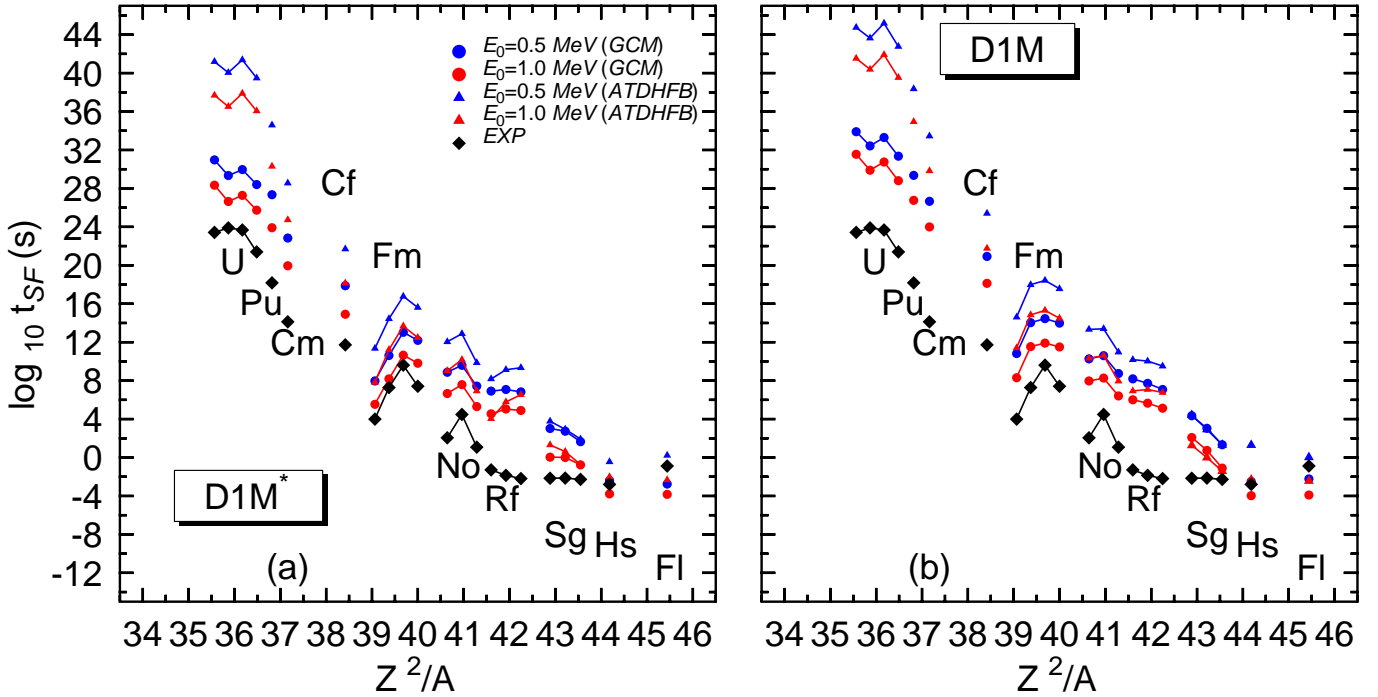


FIG. 2: (Color online) The spontaneous fission half-lives t_{SF} obtained for the nuclei $^{232-238}\text{U}$, ^{240}Pu , ^{248}Cm , ^{250}Cf , $^{250-256}\text{Fm}$, $^{252-256}\text{No}$, $^{256-260}\text{Rf}$, $^{258-262}\text{Sg}$, ^{264}Hs and ^{286}Fl within the GCM and ATDHF schemes are depicted, as functions of the fissility-related parameter Z^2/A , in panel (a) for the Gogny-D1M* and in panel (b) for the Gogny-D1M EDFs. They are compared with the corresponding experimental data [86, 87]. Theoretical results are shown for $E_0 = 0.5$ MeV and $E_0 = 1.0$ MeV. For more details, see the main text.

in the collective masses have been softened using a three point filter to facilitate the numerical evaluation of the required integrals [17–19]. Those wiggles are due to level crossings in the single particle spectrum. As the inertia is computed using the “perturbative” approximation the effect of level crossings is more intense than in the case of an exact evaluation of the inertia.

In order to examine the competition between spontaneous fission and α -decay, we have computed the α -decay half-lives t_α using the Viola-Seaborg formula [15]

$$\log_{10} t_\alpha = \frac{AZ + B}{\sqrt{Q_\alpha}} + CZ + D \quad (5)$$

with the parameters A , B , C and D given in Ref. [16]. The Q_α value is obtained in each case from the calculated binding energies.

We have kept axial symmetry as a selfconsistent symmetry along the whole fission path of each of the studied nuclei to reduce the already substantial computational effort. We are aware of the role of triaxiality around the top of the inner fission barrier, but as discussed below it seems to have little impact on spontaneous fission half-lives in the nuclei where this effect has been studied. Typically, once the γ degree of freedom is taken into account, the inner barriers are a few (2-3) MeV smaller than the axial ones [17, 42, 57, 61]. Nevertheless, it has also been shown that the lowering of the inner barrier comes along with a decrease of the level density, and therefore of the

pairing correlations that leads to an increase in the collective inertia [42, 54, 56] that tends to compensate the effect of the lower barrier in the final value of the action. As a consequence, the impact of triaxiality on the spontaneous fission half-lives is very limited in the nuclei considered, mostly actinides and $N < 190$. Although a careful analysis is still required, we expect that the same trend will be valid for all the nuclei considered in this work. Moreover, in the framework of the least action approach, it has been shown that pairing fluctuations play a key role to improve the comparison between the theoretical and experimental t_{SF} values [23, 24, 96] and, at the same time, they can restore axial symmetry along the fission path [97, 98].

Concerning the D1M* parametrization there has been some debate in the literature [99] about the spurious finite-size instabilities that appear when this parametrization is used in HFB solvers in coordinate space. As discussed at length in [100] we have never observed such a behavior in our calculations using the harmonic oscillator basis. The conclusion of [100, 101] is that the ultraviolet cutoff characteristic of the harmonic oscillator basis regularizes the spuriousities of the parametrization. Nevertheless, we have carried out some convergence tests with the basis size for the binding energy and found that the energy gains obtained with D1M* are very close to the ones of D1M that is supposed to be free from spuriousities [99]. The similitude between the D1M and

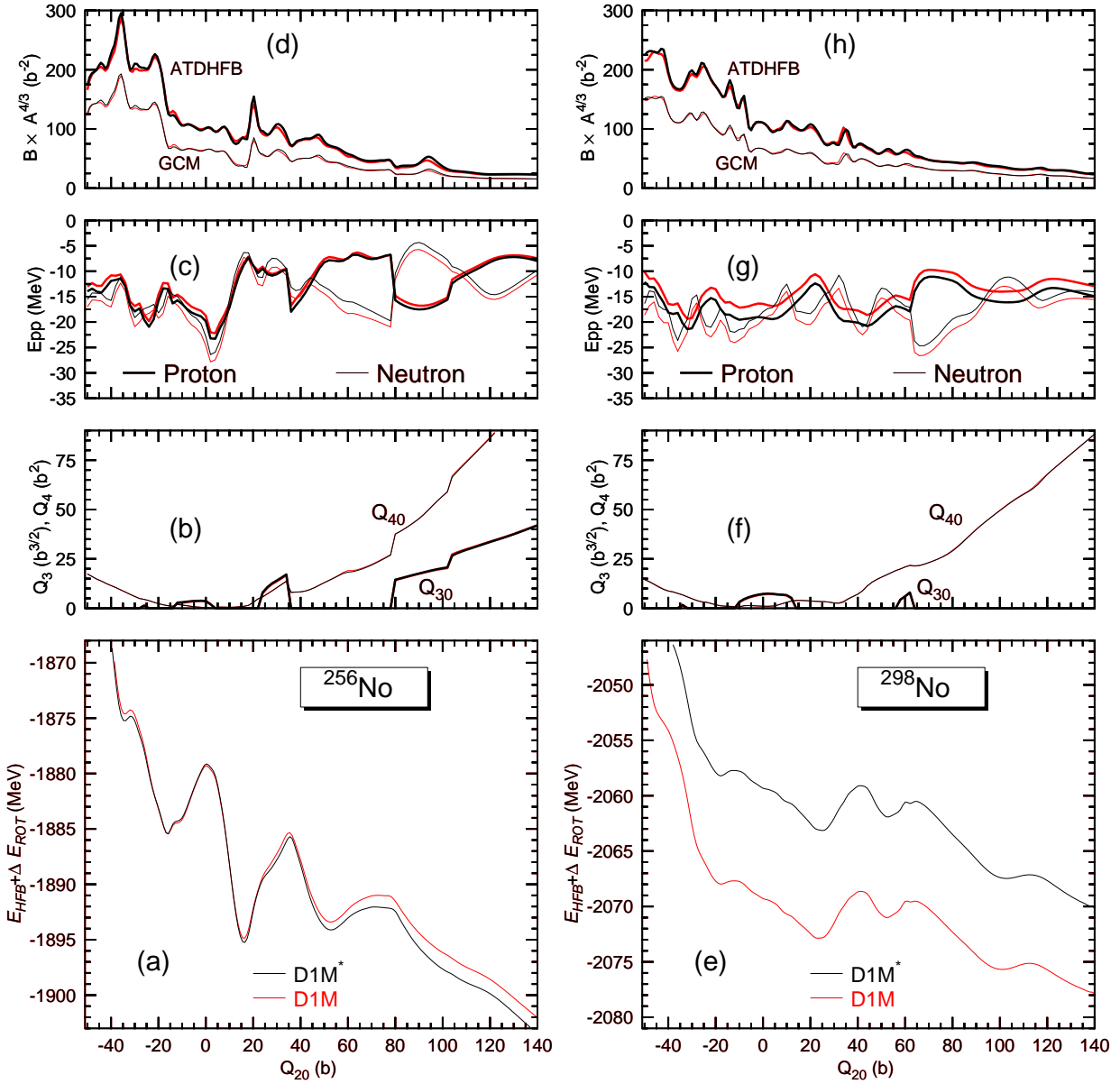


FIG. 3: (Color online) The HFB plus the zero point rotational energies obtained for the nucleus ^{256}No (^{298}No) are plotted in panel (a) [panel (e)] as functions of the quadrupole moment Q_{20} . The octupole (thick lines) and hexadecupole (thin lines) moments are plotted in panel (b) [panel (f)]. The pairing interaction energies are depicted in panel (c) [panel (g)] for protons (thick lines) and neutrons (thin lines). The collective masses obtained within the ATDHFB (thick lines) and GCM (thin lines) schemes are plotted in panel (d) [panel (h)]. Results have been obtained with the parametrizations D1M (red curves) and D1M* (black curves) of the Gogny-EDF. For more details, see the main text.

D1M* results obtained in this paper for nuclei close to the stability line (see, Sec. III) allow us to conclude that our calculations are free from spurious effects.

III. DISCUSSION OF THE RESULTS

In this section, we present the results of our fission calculations with Gogny-D1M*. In Sec. III A, we discuss the D1M* results for a set of U, Pu, Cm, Cf, Fm, No, Rf, Sg

and F1 nuclei for which experimental data are available [84–87]. In Sec. III B, we illustrate the methodology employed to compute fission observables for the nuclei ^{256}No and ^{298}No . The same methodology has been used for all the nuclei studied in this work. The aim of Secs. III A and III B is to validate the Gogny-D1M* EDF as a reasonable choice for fission studies. We will also compare our results with those obtained with the Gogny-D1M EDF. In Sec. III B, we will briefly discuss the neutron and proton single-particle energies, as functions of the

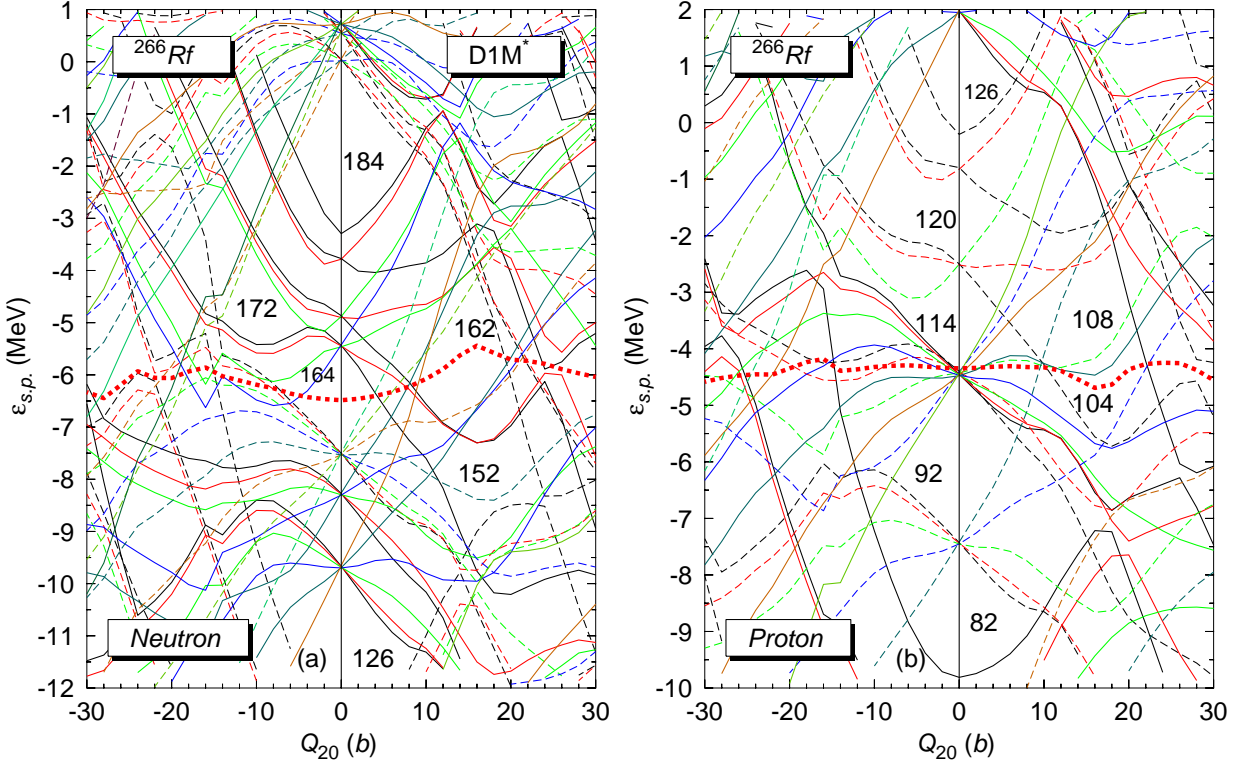


FIG. 4: (Color online) Neutron [panel (a)] and proton [panel (b)] single-particle energies, as functions of the quadrupole moment Q_{20} , for the nucleus ^{266}Rf . The Fermi levels are also plotted with a thick (red) dotted line. Results correspond to the Gogny-D1M* EDF. Solid (dashed) lines are used for positive (negative) parity states. With increasing $K = 1/2, 3/2, 5/2, \dots$ values color labels are black, red, green, blue, dark-blue, brown, dark-green, etc.

quadrupole moment Q_{20} , in the case of ^{266}Rf which is taken as an illustrative example. The systematic, provided by the Gogny-D1M* HFB approach, for the fission paths, t_{SF} and t_{α} values is presented in Sec. III C. In addition, ground state deformations, pairing correlations, two-nucleon separation energies and barrier heights are discussed in this section.

A. Heavy nuclei with known experimental data

In this section, we discuss the results obtained with the Gogny-D1M* EDF for the set of nuclei $^{232-238}\text{U}$, $^{238-244}\text{Pu}$, $^{240-248}\text{Cm}$, $^{250,252}\text{Cf}$, $^{250-256}\text{Fm}$, $^{252-256}\text{No}$, $^{256-260}\text{Rf}$, $^{258-262}\text{Sg}$, ^{264}Hs and ^{286}Fl for which, experimental data are available [84–87]. Calculations for those nuclei have been carried out along the lines discussed in Refs. [17–19] (see, also Sec. III B). Previous theoretical results, based on the parameter sets D1S and D1M, can be found in Refs. [17, 42, 47, 49].

In Table I, we compare the predicted heights $B_I^{\text{th}}(\text{D1M}^*)$ and $B_{II}^{\text{th}}(\text{D1M}^*)$ for the inner and outer barriers as well as the excitation energies $E_{II}^{\text{th}}(\text{D1M}^*)$ of the fission isomers with the experimental ones B_I^{exp} , B_{II}^{exp} and E_{II}^{exp} [84, 85]. Results obtained with the Gogny-D1M EDF [17] are also included in the table for comparison.

All the theoretical values have been obtained from the energies $E_{\text{HFB}} + E_{\text{ROT}}$ by looking at the energy differences between the ground state and the corresponding configurations along the fission paths of the studied nuclei. The calculated heights $B_I^{\text{th}}(\text{D1M}^*)$ and $B_I^{\text{th}}(\text{D1M})$ are always larger than the experimental ones. The maximal deviation $B_I^{\text{th}}(\text{D1M}) - B_I^{\text{exp}} = 4.88$ MeV occurs for ^{248}Cm while the largest difference $B_I^{\text{th}}(\text{D1M}^*) - B_I^{\text{exp}} = 4.87$ MeV is obtained for ^{246}Cm . When triaxial shapes are allowed at and in the vicinity of the first barrier we get a reduction of the barrier height. The reduction (see values in second row for the triaxial barrier heights) depends on the nucleus and goes from a few hundred keV up to ~ 3 MeV. However, the inclusion of triaxial effects cannot reconcile the theoretical values with the experimental ones. Given the reasonable agreement with the experimental t_{SF} values discussed below we can conclude that there is an unsettled issue with the comparison between the fission barrier heights obtained in the least energy framework and the experimental values (see [24] for a discussion in the context of the least action path method). It has to be considered that the experimental values are obtained in a model dependent manner from induced fission cross sections. The comparison of fission barrier heights, along with the role played by the width of the barrier and the collective inertias in the observables,

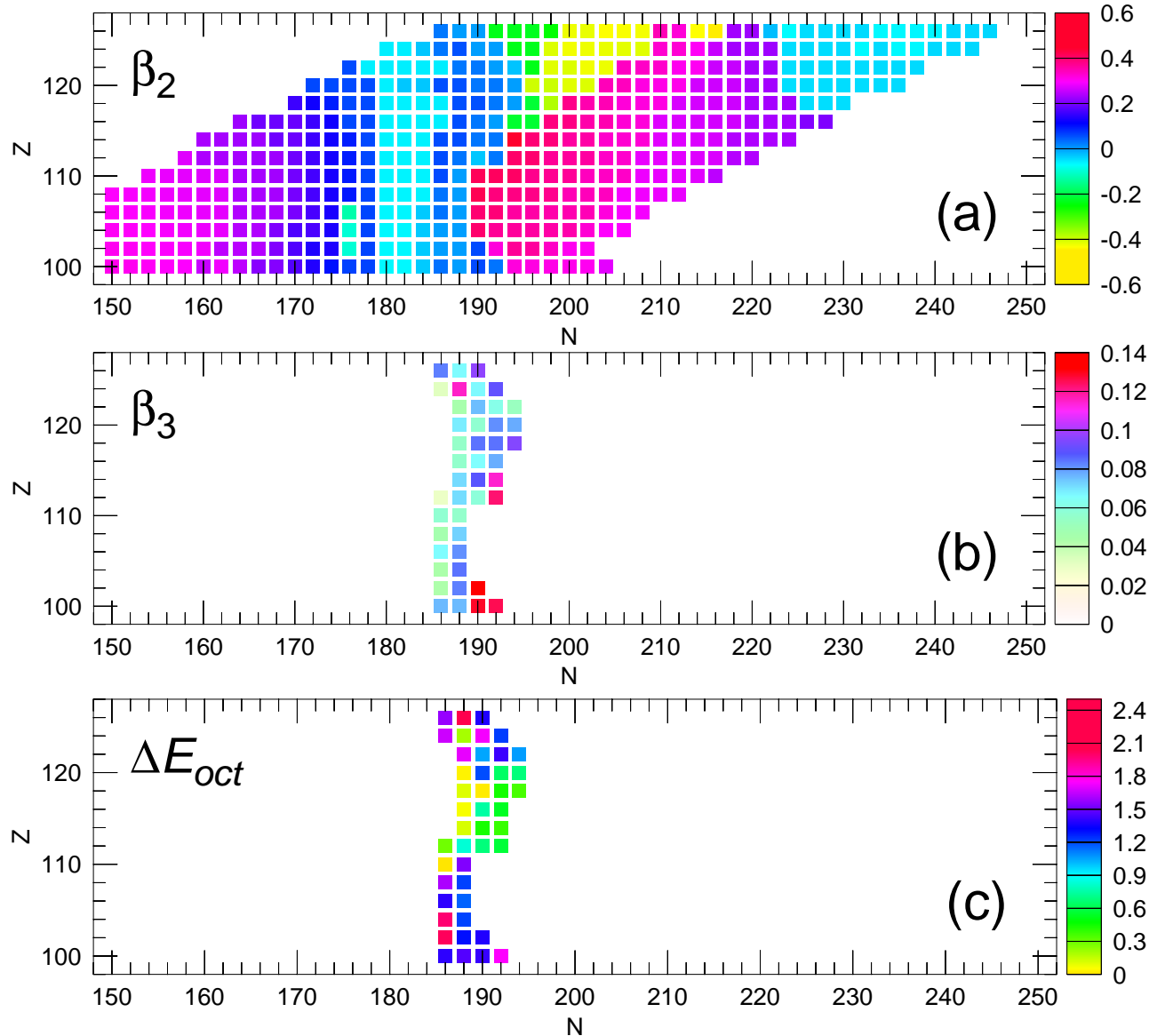


FIG. 5: (Color online) Deformation parameters β_2 [panel (a)] and β_3 [panel (b)] for the ground states of the even-even superheavy nuclei studied in this work. The octupole correlation energies ΔE_{oct} corresponding to the nuclei shown in panel (b) are plotted in panel (c). Results have been obtained with the Gogny-D1M* EDF. For more details, see the main text.

undoubtedly deserve further consideration.

The discrepancies can be attributed both to the use of an axially symmetric path and also to the uncertainties in the model dependent methodology used to extract the experimental values. It is also worth to point out that neither of the two Gogny forces were specifically fitted to fission barrier data. Nevertheless, the global trend of the computed quantities agrees reasonably well with experimental data and the results of other calculations [22, 42, 50, 58].

For the outer barrier heights and the excitation energies of the fission isomers, we obtain similar results in the two calculations, although the values obtained with D1M tend to be slightly larger than those obtained with

D1M*. This trend is a consequence of the more gentle decline observed in the Gogny-D1M fission paths for quadrupole moments $Q_{20} \geq 40$ b (see, also Sec. III B). Reflection symmetry is allowed to break along the fission path whenever it is energetically favorable. For the nuclei studied in this section, octupole correlations reduce the outer barrier heights by a few MeV. However, in the case of ^{244}Pu , we still observe deviations of up to $B_{II}^{th}(\text{D1M}) - B_{II}^{exp} = 4.75$ MeV and $B_{II}^{th}(\text{D1M}^*) - B_{II}^{exp} = 4.18$ MeV, respectively. The previous results, as well as the ones obtained with the D1S parametrization [42], seem to suggest that effects other than the ones associated with shape degrees of freedom might be required to improve the comparison with the B_{II}^{exp} values. However,

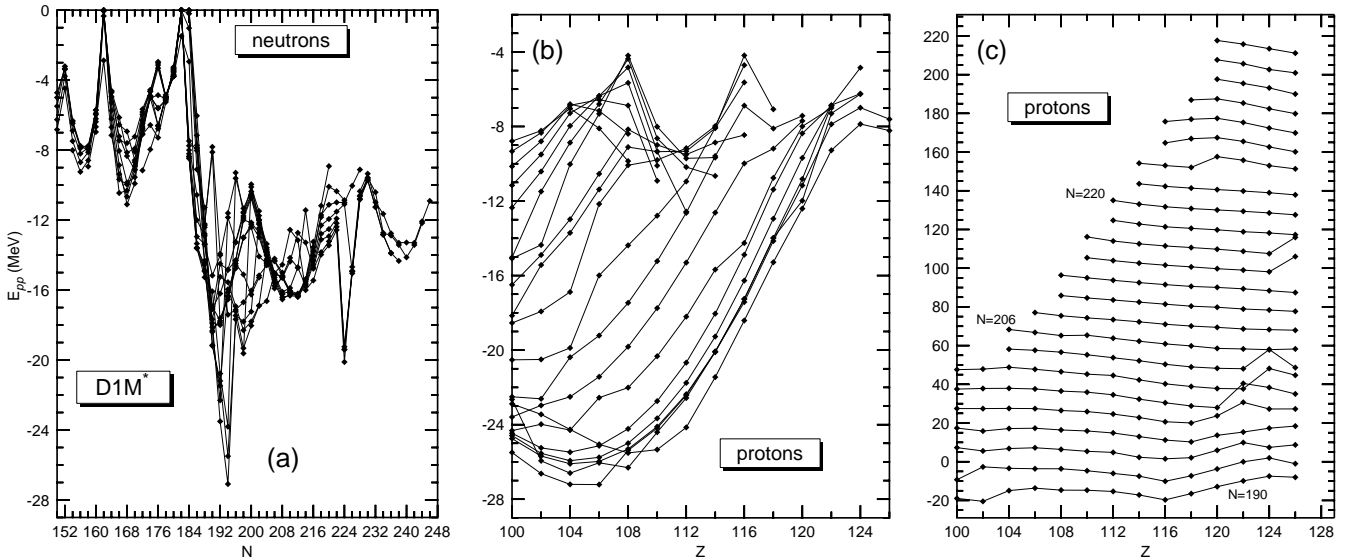


FIG. 6: The neutron and proton pairing interaction energies corresponding to the ground states of the studied nuclei are plotted in panel (a) [panels (b) and (c)]. Starting with the $N = 192$ isotones in panel (c), the curves have been shifted by 10 MeV. Results have been obtained with the Gogny-D1M* EDF. For more details, see the main text.

we would like to stress again the model dependent character of the B_{II}^{exp} values, making these quantities less reliable for a comparison with theoretical predictions, than real observables like fission half-lives. In the case of the fission isomers, we observe for ^{242}Pu differences of up to $E_{II}^{th}(\text{D1M}) - E_{II}^{exp} = 1.37$ MeV and $E_{II}^{th}(\text{D1M}^*) - E_{II}^{exp} = 0.70$ MeV, respectively.

In Fig. 2, the spontaneous fission half-lives t_{SF} obtained for the nuclei $^{232-238}\text{U}$, ^{240}Pu , ^{248}Cm , ^{250}Cf , $^{250-256}\text{Fm}$, $^{252-256}\text{No}$, $^{256-260}\text{Rf}$, $^{258-262}\text{Sg}$, ^{264}Hs and ^{286}Fl are plotted as functions of the fissility-related parameter Z^2/A . Results obtained within both the GCM and ATDHFB schemes are shown for both the Gogny-D1M* [panel (a)] and the Gogny-D1M [panel (b)] EDFs. The results are compared with the corresponding experimental data [86, 87]. Calculations have been carried out with $E_0 = 0.5$ MeV and $E_0 = 1.0$ MeV. This is a very delicate comparison as the experimental t_{SF} values span 27 orders of magnitude. Regardless of the considered Gogny-EDF, the computed half-lives display an even larger variability depending on the scheme employed. As it has already been noted in previous studies [17–19], increasing the value of E_0 improves the comparison with the experiment in both of the two schemes especially for Fm, No, Rf, Sg, Hs and Fl nuclei. It is satisfying to observe that D1M* provides the same quality of results as D1M and captures the pronounced experimental reduction in the spontaneous fission half-lives for increasing values of Z^2/A . Moreover, along isotopic chains the trend with neutron number is also reasonably well reproduced by both EDFs.

B. The nuclei ^{256}No and ^{298}No

In this section, we illustrate the methodology employed to compute the fission paths and other fission-related quantities for the nuclei ^{256}No and ^{298}No . The corresponding Gogny-D1M* HFB plus the zero point rotational energies are plotted in panels (a) and (e) of Fig. 3 as functions of the quadrupole moment Q_{20} . Results obtained with the Gogny-D1M EDF are also included in each of the panels. The zero point vibrational energies are not included in the plots as they are rather constant as functions of the quadrupole moment. However, we always consider such vibrational corrections in the computation of the t_{SF} and t_α lifetimes.

In the case of ^{256}No , the absolute minimum is located at $Q_{20} = 16\text{b}$. The fission isomer, located at $Q_{20} = 52\text{b}$, lies $E_{II}^{th}(\text{D1M}^*) = 1.16$ MeV above the ground state from which it is separated by the inner barrier the top of which, is located at $Q_{20} = 36\text{b}$ with the height $B_I^{th}(\text{D1M}^*) = 9.53$ MeV. The outer barrier with the height $B_{II}^{th}(\text{D1M}^*) = 3.20$ MeV is found at $Q_{20} = 72\text{b}$. For the Gogny-D1M fission path the absolute minimum is also located at $Q_{20} = 16\text{b}$ while $B_I^{th}(\text{D1M}) = 9.46$ MeV ($Q_{20} = 36\text{b}$), $E_{II}^{th}(\text{D1M}) = 1.51$ MeV ($Q_{20} = 52\text{b}$) and $B_{II}^{th}(\text{D1M}) = 3.90$ MeV ($Q_{20} = 72\text{b}$).

For the neutron-rich nucleus ^{298}No , the absolute minimum is located at $Q_{20} = 24\text{b}$. We have obtained $B_I^{th}(\text{D1M}^*) = 4.00$ MeV ($Q_{20} = 42\text{b}$), $E_{II}^{th}(\text{D1M}^*) = 1.21$ MeV ($Q_{20} = 52\text{b}$) and $B_{II}^{th}(\text{D1M}^*) = 2.53$ MeV ($Q_{20} = 60\text{b}$). On the other hand, for the Gogny-D1M fission path the absolute minimum is also located at $Q_{20} = 24\text{b}$ while $B_I^{th}(\text{D1M}) = 4.20$ MeV ($Q_{20} = 42\text{b}$), $E_{II}^{th}(\text{D1M}) = 1.85$ MeV ($Q_{20} = 52\text{b}$) and $B_{II}^{th}(\text{D1M}) = 3.32$ MeV ($Q_{20} = 60\text{b}$).

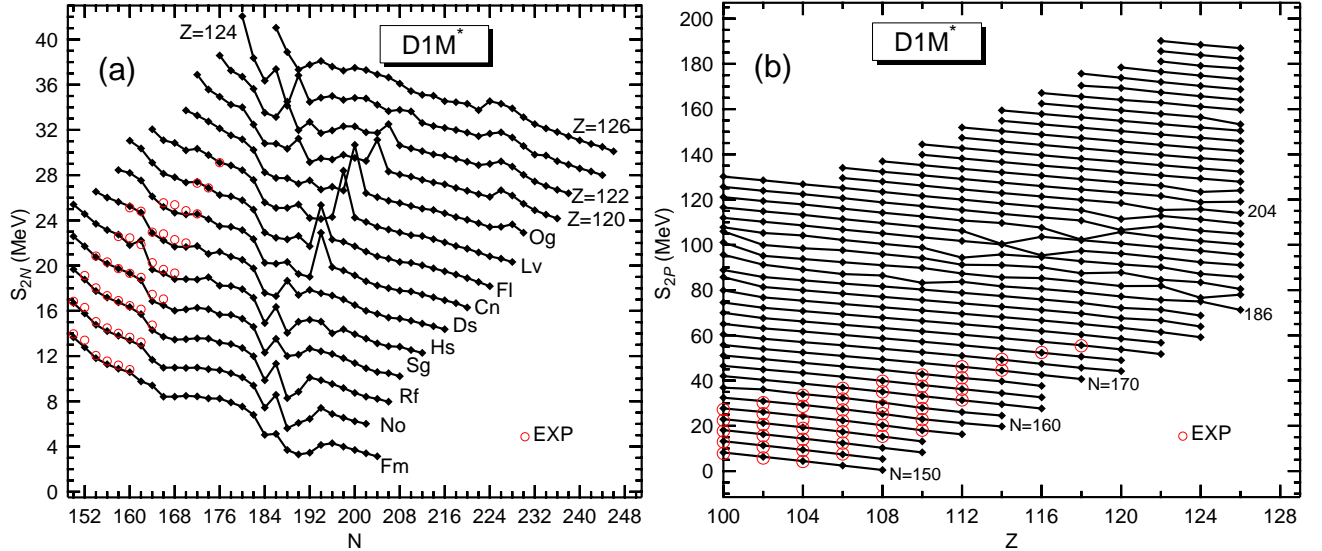


FIG. 7: (Color online) The two-neutron (two-proton) separation energies are plotted as functions of the neutron number N (proton number Z) in panel (a) [panel (b)]. Starting with the $Z = 102$ isotopes in panel (a) [$N = 152$ isotones in panel (b)] the curves have been shifted by 2 MeV (4 MeV). Results have been obtained with the Gogny-D1M* EDF. Experimental data have been taken from Ref. [110]. For more details, see the main text.

From the previous results one realizes that, for both ^{256}No and ^{298}No , the topology of the fission paths obtained with the D1M and D1M* Gogny-EDFs are quite similar albeit with a more gentle decline of the former as compared with the latter for quadrupole moments $Q_{20} \geq 40\text{b}$ [see, for example, panel (a)]. However, in the case of ^{298}No , there is a pronounced under-binding for all the configurations along the Gogny-D1M* path. Such a shift with increasing neutron number N along an isotopic chain has been pointed out in Ref. [81] and it is a direct consequence of the different density dependence of the symmetry energy in the two EDFs.

The octupole and hexadecupole moments obtained for ^{256}No and ^{298}No are plotted in panels (b) and (f) of the figure. In the case of ^{256}No , octupole deformed shapes are energetically favored for $-14\text{b} \leq Q_{20} \leq 4\text{ b}$ and $24\text{b} \leq Q_{20} \leq 34\text{ b}$. Octupole correlations also play a prominent role for $Q_{20} \geq 80\text{b}$ leading to a reflection-asymmetric outer sector of the fission path much lower in energy than the symmetric (i.e., $Q_{30} = 0$) one. In the case of ^{298}No , octupole deformed shapes play a role around both the spherical configuration and $Q_{20} = 60\text{b}$ while for larger quadrupole moments the (minimal energy) path corresponds to reflection-symmetric shapes.

The pairing interaction energies $E_{pp} = -1/2\text{Tr}(\Delta\kappa^*)$ [39] are depicted in panels (c) and (g) of Fig. 3. The proton and neutron pairing content of the two Gogny-EDFs is similar because the two combinations of parameters $W_i - B_i - H_i + M_i$ ($i = 1, 2$) of the finite-range part of the Gogny-EDF [40] which govern the pairing strength have been kept fixed to their D1M values in the fitting protocol of D1M* [81]. The collective masses are plotted in panels (d) and (h). Their evolution, as functions of

Q_{20} , is well correlated with the one of the pairing energies shown in panels (c) and (g). Regardless of the considered EDF, the GCM and ATDHFB masses exhibit a similar pattern, though the values of the latter are always larger than the former. As a consequence, the action Eq. (4) computed within the ATDHFB scheme is larger than the GCM one. Those differences can represent a change of several orders of magnitude in the predicted fission half-lives Eq. (3) [17–24]. This is the reason to consider both kinds of collective masses in this work. For example, in the case of ^{256}No and $E_0 = 0.5$ MeV, we have obtained the values $\log_{10}t_{\text{SF}}^{\text{GCM}} = 8.88$ and $\log_{10}t_{\text{SF}}^{\text{ATDHFB}} = 12.04$ with the Gogny-D1M* EDF. For the same nucleus, the values obtained with D1M are $\log_{10}t_{\text{SF}}^{\text{GCM}} = 10.53$ and $\log_{10}t_{\text{SF}}^{\text{ATDHFB}} = 13.72$. A larger E_0 value leads to a reduction in the predicted fission half-lives. For ^{256}No and $E_0 = 1.0$ MeV, we have obtained $\log_{10}t_{\text{SF}}^{\text{GCM}} = 6.66$ and $\log_{10}t_{\text{SF}}^{\text{ATDHFB}} = 9.02$ with D1M* while the corresponding values with D1M are $\log_{10}t_{\text{SF}}^{\text{GCM}} = 8.18$ and $\log_{10}t_{\text{SF}}^{\text{ATDHFB}} = 10.67$.

To summarize the results already discussed in Secs. III A and III B, it has been shown that, in spite of the theoretical uncertainties in the models employed to describe the considered quantities, the Gogny-D1M* HFB framework describes reasonably well the trend with mass number in the studied observables and also that its predictions compare well with those obtained with the parametrization D1M. This validates the use of the D1M* parameter set to study the systematic of the fission paths as well as other relevant quantities for the even-even nuclei shown in Fig. 1.

Before concluding this section, we turn our attention to single-particle properties. As it is well known, the

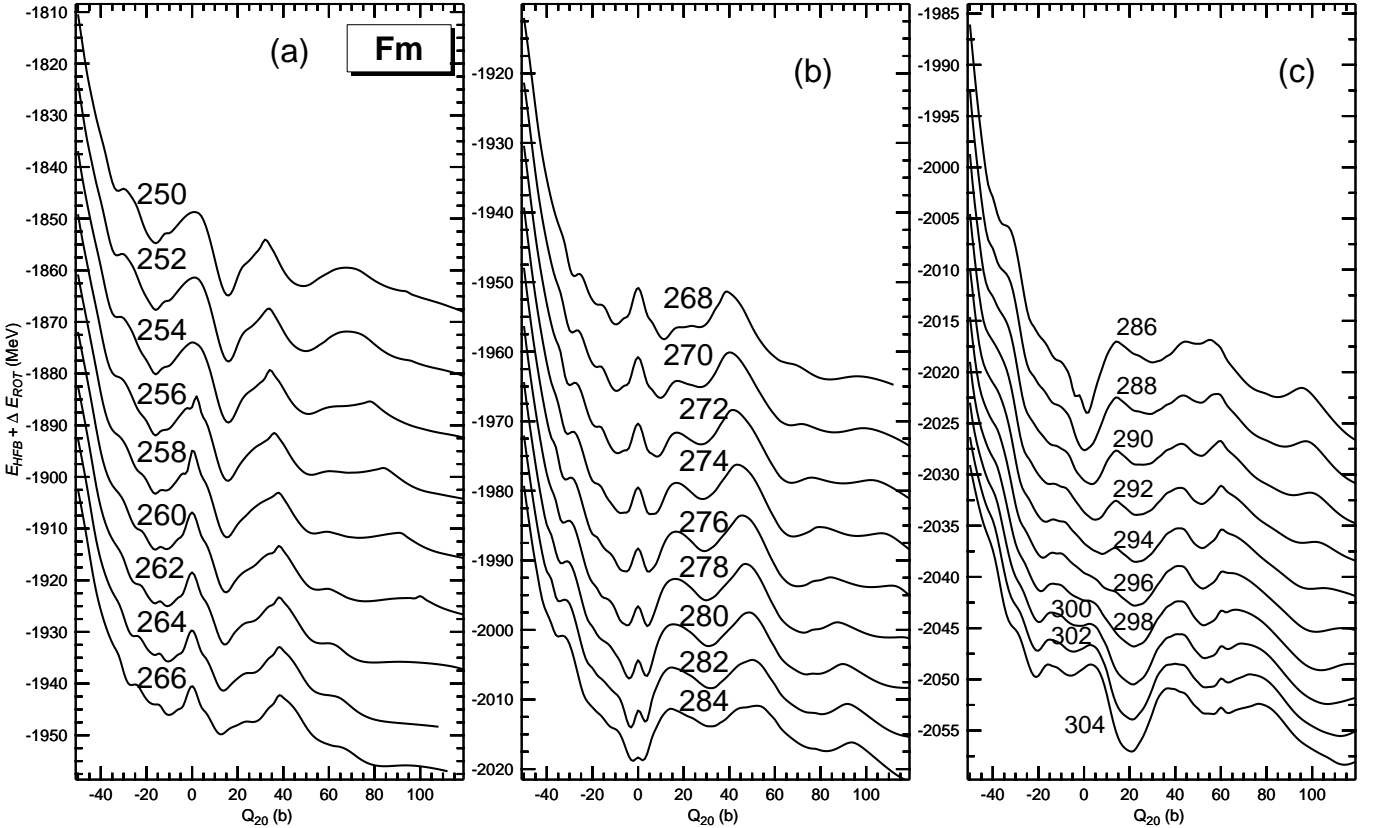


FIG. 8: The HFB plus the zero point rotational energies, obtained with the Gogny-D1M* EDF, are plotted as functions of the quadrupole moment Q_{20} for the nuclei $^{250-304}\text{Fm}$. Starting from ^{252}Fm [panel (a)], ^{270}Fm [panel (b)] and ^{288}Fm [panel (c)], the curves have been successively shifted by 2.5 MeV in order to accommodate them in a single plot. Note that the energy scales span different ranges in each panel. For more details, see the main text.

existence of minima as a function of some collective parameter is strongly linked to the existence of regions with low single-particle densities (Jahn-Teller effect). Therefore, plotting single-particle energies (SPEs) as a function of the quadrupole deformation helps us to identify regions where energy gaps favor the appearance of deformed minima. As in our mean-field calculations we solve the full HFB equations, the only quantities that can be properly defined are the quasiparticle energies [39]. However, in order to have the usual Nilsson-like type of diagram we have chosen to plot the eigenvalues of the Routhian $h = t + \Gamma - \lambda_{Q_{20}} Q_{20} - \lambda_{Q_{30}} Q_{30}$, with t being the kinetic energy and Γ the Hartree-Fock field. The term $\lambda_{Q_{20}} Q_{20} + \lambda_{Q_{30}} Q_{30}$ contains the Lagrange multipliers used to enforce the corresponding quadrupole and octupole constraints.

The neutron and proton SPEs, computed with the Gogny-D1M* EDF, are plotted in Fig. 4 for ^{266}Rf . As can be seen from panel (a), a spherical sub-shell is predicted at $N = 164$. However, the spherical shell closures at $N = 126$ and $N = 184$ are much more pronounced. Note, that in our calculations the spherical magic number next to $N = 184$ is $N = 228$. Prolate (oblate) gaps are observed at $N = 152$ and $N = 162$ ($N = 172$). In

the case of protons [panel (b)], we observe a sub-shell at $Z = 114$ smaller than the shell closures at $Z = 92$, 120 and 126. Prolate proton gaps are also found at $Z = 104$ and $Z = 108$. Similar results are obtained with the Gogny-D1M EDF and will not be shown here. The previous results also agree well with those obtained with the Gogny-D1S parametrization [49]. For a discussion of spherical and deformed shell gaps in superheavy nuclei within the relativistic mean-field (RMF) and Skyrme-EDF approximations the reader is referred, for example, to Refs. [102, 103].

C. Systematic of the fission paths and spontaneous fission half-lives

For each of the even-even nuclei shown in Fig. 1, we have performed a systematic analysis of the fission path, obtained with the Gogny-D1M* EDF, along the lines discussed in Sec. III B. Let us first turn our attention to the ground state quadrupole β_2 Eq.(1) and octupole β_3 Eq. (2) deformation parameters. They are shown in panels (a) and (b) of Fig. 5. A more detailed description of the fission paths will be presented later on in the paper.

As can be seen from panel (a) of the figure, well deformed prolate ground states ($0.05 \leq \beta_2 \leq 0.29$) are obtained for nuclei with proton and neutron numbers $100 \leq Z \leq 122$ and $150 \leq N \leq 178$. There are a few exceptions in the region corresponding to the well deformed oblate nuclei ^{278}No , ^{280}Rf , ^{282}Sg and $^{300}\text{122}$. A region of weakly deformed and/or spherical ground states ($-0.06 \leq \beta_2 \leq 0.06$) emerges as we approach $N=184$ and roughly extends up to $N = 192$ -194. Beyond $N=192$ -194, our calculations predict a region with pronounced prolate ($0.21 \leq \beta_2 \leq 0.37$) deformations. A small pocket of strongly oblate ($-0.41 \leq \beta_2 \leq -0.35$) systems is also found in this region. Finally, weakly oblate ($\beta_2 \approx -0.04$) ground states are found for $118 \leq Z \leq 126$ and $224 \leq N \leq 246$. In our calculations, specially with increasing Z values, the fission paths obtained for some neutron-rich nuclei exhibit a very complex topology with several competing minima. Similar results have been obtained in previous works [49, 55, 104]. Exception made of a small number of cases, in those situations where the identification of the absolute minimum of the fission path becomes more involved, we have taken the deepest minimum closest to sphericity as the ground state of the system [104].

In most of the cases the ground state is reflection-symmetric, as can be seen in panel (b) of Fig. 5. However, octupole deformed ground states are found for a small set of nuclei with neutron numbers $186 \leq N \leq 194$. On the one hand, this agrees well, with previous results obtained with the Gogny-D1S [49] and BCPM [55] EDFs as well as within the Mac-Mic model [105]. In particular, all these models predict the existence of an island of octupole deformed nuclei around $N \approx 196$. Previous calculations based on the Skyrme-SLy6 EDF [52] and four different RMF models [106] also agree on the existence of such islands of octupolarity in neutron-rich low- Z superheavy nuclei. However, the Skyrme-SLy6 and RMF calculations do not predict octupole deformed ground states for nuclei with atomic number $Z \geq 110$. We have computed the octupole correlation energy [106]

$$\Delta E_{oct} = |E(Q_{20}, Q_{30}) - E(Q'_{20}, Q'_{30} = 0)| \quad (6)$$

where $E(Q_{20}, Q_{30})$ and $E(Q'_{20}, Q'_{30} = 0)$ represent the binding energies of a given nucleus at the octupole deformed absolute minimum of the fission path and the absolute minimum obtained in reflection-symmetric calculations, respectively. The values of ΔE_{oct} are plotted in panel (c) of Fig. 5. As can be seen, in our Gogny-D1M* calculations the largest octupole correlation energies are around 2 MeV. For example, we have obtained $\Delta E_{oct} = 2.02, 1.98$ and 2.04 MeV for the nuclei ^{288}No , ^{290}Rf and $^{314}\text{126}$.

The average values of higher multipolarity moments (for example, \hat{Q}_{40} and \hat{Q}_{60}) are determined by the self-consistent minimization procedure of the HFB energy. We have found, that the global trends observed in the corresponding β_4 and β_6 parameters compare well with the ones obtained in previous studies [49, 55, 105, 107].

The neutron pairing interaction energies corresponding to the ground states of the studied nuclei are plotted in panel (a) of Fig. 6. They vanish around $N = 162$ and 184 , which correlates well with the low densities of neutron SPEs in panel (a) of Fig. 4. The smaller pairing correlations at $N = 162$ are consistent with the prolate deformed ground states obtained for the isotones ^{262}Fm , ^{264}No , ^{266}Rf , ^{268}Sg , ^{270}Hs , ^{272}Ds , ^{274}Cn and ^{276}Fl [see, panel (a) of Fig. 5]. On the other hand, the large pairing energies around $N = 156, 168, 194, 210, 224$ and 240 are associated with regions of high density of SPE levels.

The pattern displayed by the proton pairing energies, shown in panels (b) and (c) of Fig. 6, is more involved than the one of the neutron pairing energies due to the fact that, for a given Z value and depending on neutron number, the isotopes can be prolate, oblate and/or nearly spherical. The smaller pairing energies obtained for $Z = 104, 108, 116, 120$ and 126 [panel (b)] are related to regions with low proton level densities. On the other hand, beyond $N = 188$ the proton pairing energies exhibit a change in tendency which can be associated to sudden ground state shape transitions. The proton pairing energies for $N \geq 190$ are depicted in panel (c). In order to avoid line crossings, starting with the $N = 192$ isotones, the curves have been shifted by 10 MeV. In the case of the $N = 200$ isotones, for example, the proton pairing energies decrease for $100 \leq Z \leq 120$ and increase at $Z = 122$. Such a behavior results from a prolate-to-oblate shape transition [see, panel (a) of Fig. 5].

The two-neutron separation energies S_{2N} are depicted in panel (a) of Fig. 7 as functions of the neutron number N . Starting with the No isotopes ($Z = 102$), the curves have been shifted by 2 MeV. With this choice of the energy shift the crossing of some lines is avoided and the general pattern of the S_{2N} values is better revealed. As expected, the two-neutron separation energies decrease with increasing neutron number since we move towards the corresponding two-neutron driplines. For each of the considered isotopic chains, we have extended our calculations to very neutron-rich isotopes with S_{2N} as low as ≈ 4 MeV. For example, for the neutron-rich nuclei ^{304}Fm , ^{314}Sg , ^{332}Cn , $^{360}\text{122}$ and $^{372}\text{126}$ we have obtained $S_{2N} = 3.13, 4.22, 4.30, 4.40$ and 4.10 MeV, respectively. As can be seen from the figure, there is a sudden decline in the S_{2N} values around $N = 162$ and $N = 184$. On the other hand prominent peaks (up to ≈ 4 MeV higher than their neighbors' values) have been obtained in the case of Cn, Fl, Lv, Og and $Z=120$ isotopes at $N = 194, 194, 198, 200$ and 204 , respectively. Those peaks reflect the sensitivity of the S_{2N} values with respect to the ground state shapes of the nuclei involved in their computation. In particular, for the already mentioned neutron numbers the peaks in the two-neutron separation energies are associated with sudden ground state shape changes [see, panel (a) of Fig. 5]. A more realistic treatment of those peaks as well as the jumps when crossing shell closures requires the inclusion of dynamical correlations (i.e., symmetry-projected quadrupole configuration mixing [108, 109])

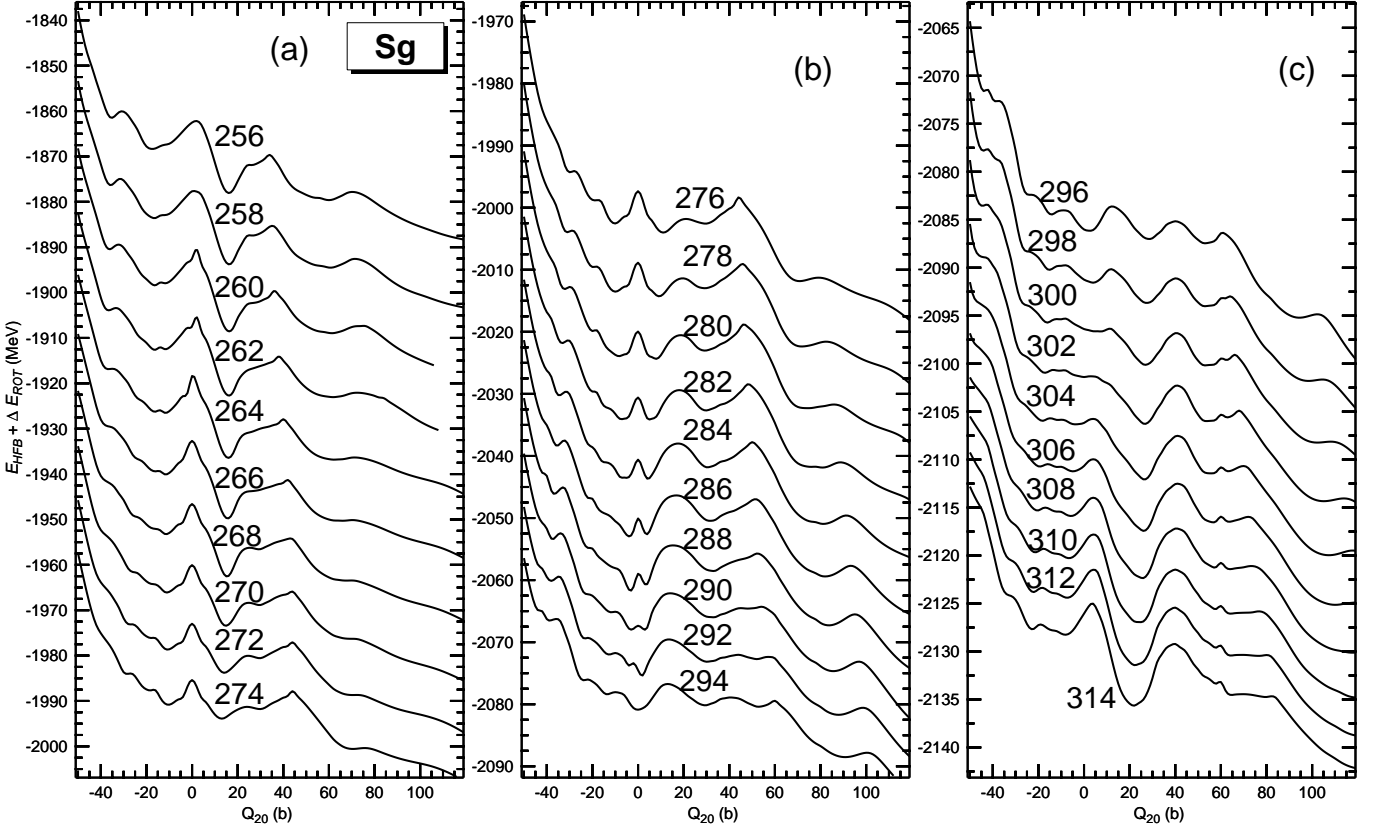


FIG. 9: The HFB plus the zero point rotational energies, obtained with the Gogny-D1M* EDF, are plotted as functions of the quadrupole moment Q_{20} for the nuclei $^{256-314}\text{Sg}$. Starting from ^{258}Sg [panel (a)], ^{278}Sg [panel (b)] and ^{298}Sg [panel (c)], the curves have been successively shifted by 2.5 MeV in order to accommodate them in a single plot. Note that the energy scales span different ranges in each panel. For more details, see the main text.

which are out of the scope of the present study. It is satisfying to observe that the Gogny-D1M* calculations reproduce reasonably well the available experimental data [110]. Moreover, the Gogny-D1M* S_{2N} values compare well with the ones obtained with the D1M parametrization. For example, for the isotopes $^{250-256}\text{Fm}$, we have obtained $S_{2N} = 13.65, 12.77, 11.81$, and 11.26 MeV with D1M* and $S_{2N} = 14.00, 13.14, 12.23$ and 11.73 MeV with D1M. All these theoretical values should be compared with the experimental ones [110] i.e., $S_{2N} = 13.97, 13.40, 12.06$ and 11.56 MeV. On the other hand, for the very neutron-rich isotopes $^{302,304}\text{Fm}$ we have obtained $S_{2N} = 3.39$ and 3.12 MeV with D1M* and $S_{2N} = 4.00$ and 3.70 MeV with D1M.

The two-proton separation energies S_{2P} are depicted in panel (b) of Fig. 7 as functions of the proton number Z . Starting with the $N = 152$ isotones, the curves have been shifted by 4 MeV. As can be seen, with few exceptions, the S_{2P} values display a structureless behavior. Only for isotones with $186 \leq N \leq 204$, we find some irregularities associated with sudden shape transitions. As with the two-neutron separation energies, a more realistic treatment of those irregularities requires the inclusion of dynamical correlations [108, 109]. Along isotonic chains,

the S_{2P} values decrease with increasing proton number as one moves towards the two-proton driplines. In our calculations, the nuclei ^{274}Fl , ^{280}Lv , $^{298}\text{122}$, $^{304}\text{124}$, $^{306}\text{124}$ and $^{312}\text{126}$ are slightly unbound with $S_{2P} = -0.28, -0.35, -0.28, -0.83, -0.10$ and -0.77 MeV, respectively. Our calculations agree well with the available experimental data [110] as well as with results obtained with the D1M parametrization. For example, for $^{250-256}\text{Fm}$, we have obtained $S_{2P} = 8.20, 9.21, 10.11$, and 10.95 MeV with D1M* and $S_{2P} = 7.62, 8.59, 9.47$, and 10.31 MeV with D1M. The previous values should be compared with the experimental ones [110] i.e., $S_{2P} = 7.74, 8.93, 9.71$ and 10.43 MeV.

The comparison of the S_{2N} and S_{2P} values, obtained with the Gogny-D1M* EDF, with the available experimental data provides the rms values $\sigma(S_{2N}) = 0.36$ MeV and $\sigma(S_{2P}) = 0.52$ MeV.

Let us perform a more detailed description of the fission paths of the studied nuclei. We stress, that reflection symmetry has been allowed to break at any stage of our calculations. As a consequence, octupole deformed shapes have been taken into account, whenever they are favored energetically, along the minimal energy (one-dimensional projected) fission paths discussed in what

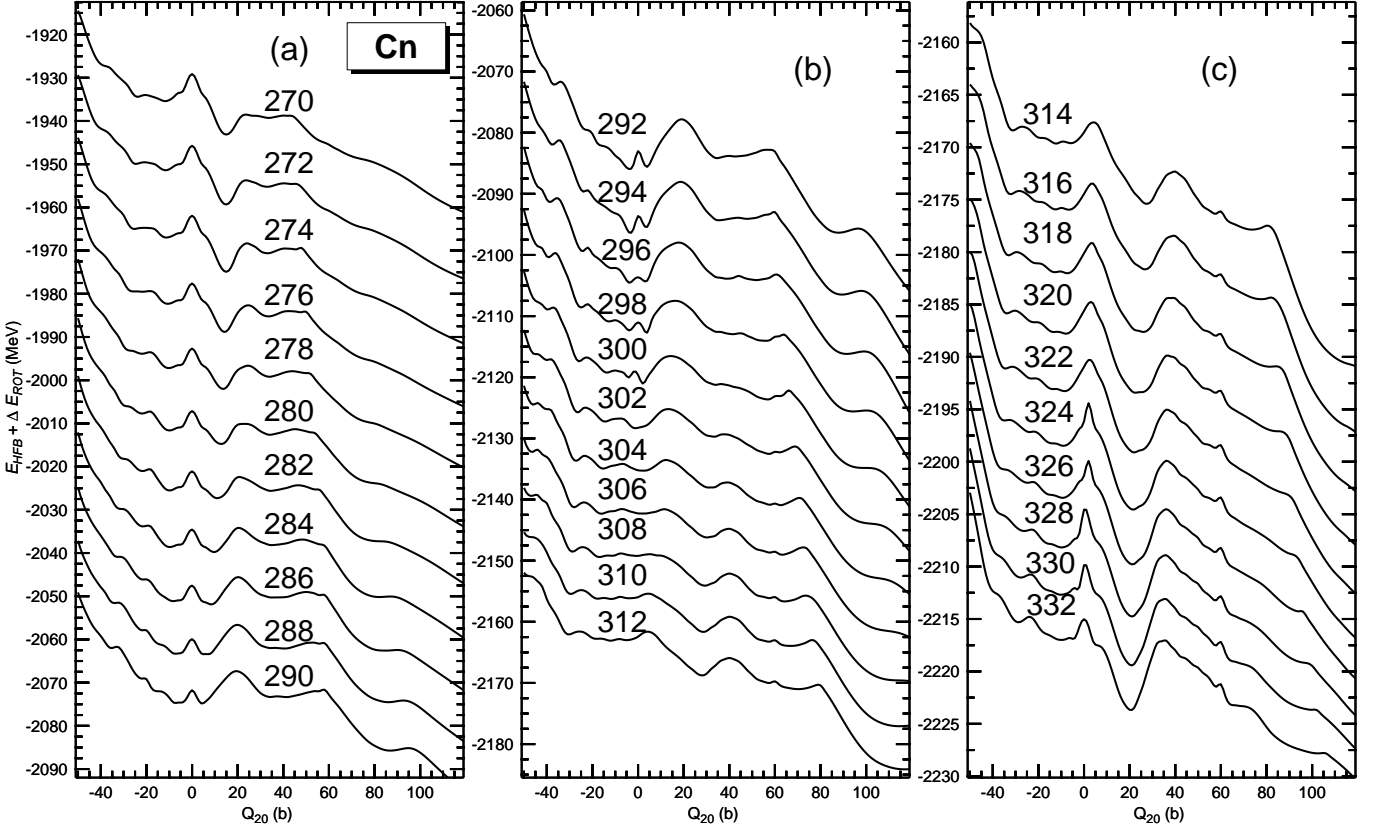


FIG. 10: The HFB plus the zero point rotational energies, obtained with the Gogny-D1M* EDF, are plotted as functions of the quadrupole moment Q_{20} for the nuclei $^{270-332}\text{Cn}$. Starting from ^{272}Cn [panel (a)], ^{294}Cn [panel (b)] and ^{316}Cn [panel (c)], the curves have been successively shifted by 2.5 MeV in order to accommodate them in a single plot. Note that the energy scales span different ranges in each panel. For more details, see the main text.

follows as functions of the driving quadrupole moment Q_{20} .

The HFB plus the zero point rotational energies, are plotted in Fig. 8 for $^{250-304}\text{Fm}$. The main features of the fission paths for $150 \leq N \leq 170$ are a prolate ground state and a wide fission barrier. Shallow fission isomers and outer barriers have been obtained for the lighter isotopes but, they disappear with increasing N . A shoulder develops between the ground state and the top of the fission barrier becoming more apparent at $N=170$. The isotopes with $172 \leq N \leq 178$ are still prolate though with smaller deformations. Here, the shoulder becomes a deeper prolate local minimum and the fission barriers are two-humped.

For $180 \leq N \leq 192$, the ground states are weakly deformed or spherical. In particular, $^{280-284}\text{Fm}$ are predicted to be weakly oblate. All those nuclei, become spherical at the (intrinsic) HFB level as their neutron numbers are close to $N=184$, which is predicted to be a magic neutron number in our Gogny-D1M* calculations as well as with the D1M parametrization. The nonzero ground state Q_{20} value is a direct consequence of the rotational energy correction that shifts spherical HFB minima to nonzero quadrupole moments

[17, 94, 95, 111, 112]. The prolate local minimum decreases its excitation energy with increasing N . Starting at $N=186$ the top of the second barrier develops an additional minimum and the fission paths for $N>186$ become three-humped. The prolate local minimum becomes the ground state for $194 \leq N \leq 204$. The associated prolate wells increase their depth and two-humped barriers determine the stability of these isotopes against fission. Similar results have been obtained for the No and Rf chains.

The HFB plus the zero point rotational energies, are shown in Fig. 9 for $^{256-314}\text{Sg}$. Many of the features obtained for the Fm, No and Rf nuclei are still present for the Sg isotopes. For example, the nuclei with $150 \leq N \leq 170$ are prolate with wide barriers. The shallow fission isomers drive the existence of the outer barriers and disappear with increasing N . A shoulder emerges between the ground state and the top of the fission barrier for ^{268}Sg and becomes more apparent for ^{276}Sg . The prolate deformations are further reduced for $172 \leq N \leq 178$, exception made of the oblate ground state obtained for ^{282}Sg . With increasing N the shoulder becomes a prolate local minimum and the fission barriers are two-humped.

For $180 \leq N \leq 188$, the ground states are weakly de-

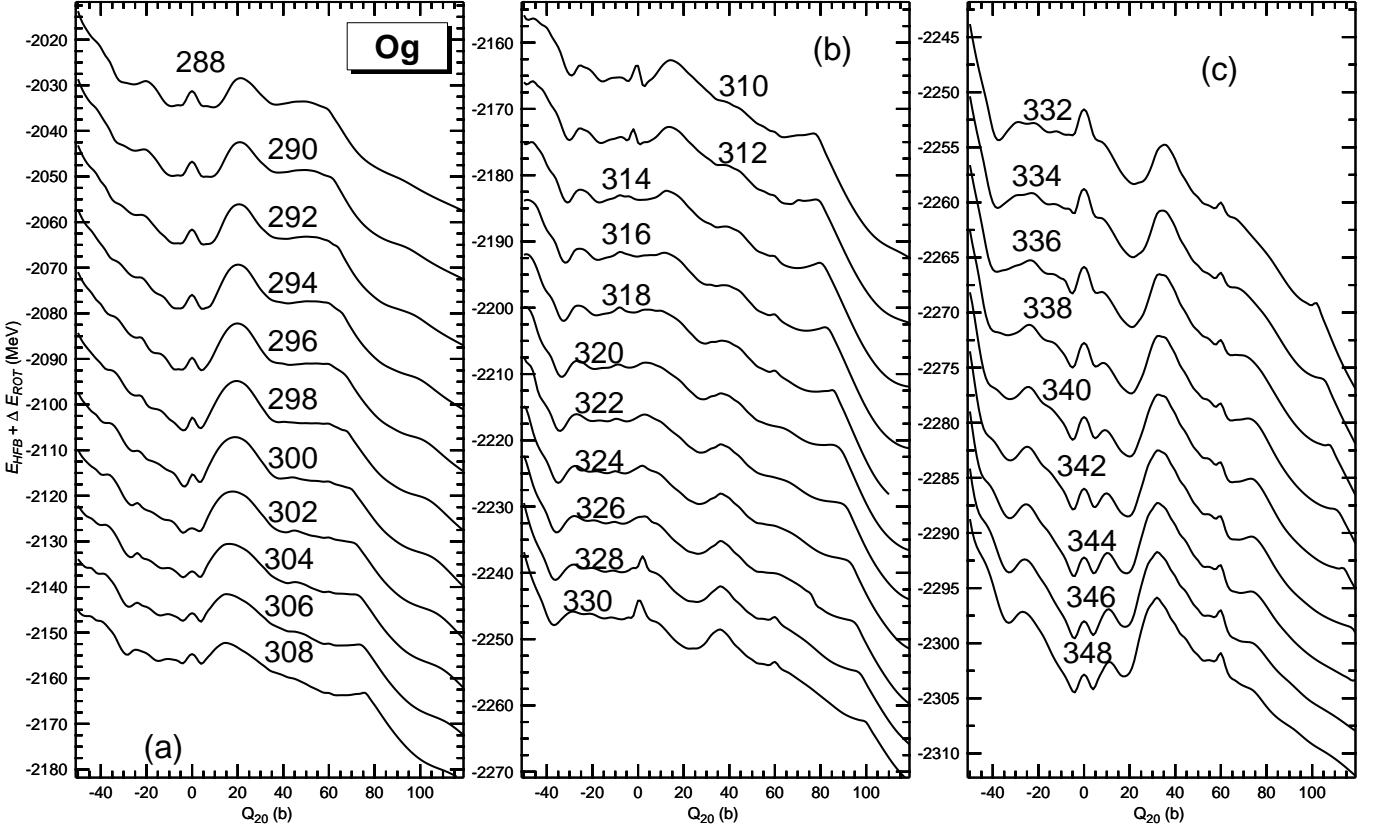


FIG. 11: The HFB plus the zero point rotational energies, obtained with the Gogny-D1M* EDF, are plotted as functions of the quadrupole moment Q_{20} for the nuclei $^{288-348}\text{Og}$. Starting from ^{290}Og [panel (a)], ^{312}Og [panel (b)] and ^{334}Og [panel (c)], the curves have been successively shifted by 2.5 MeV in order to accommodate them in a single plot. Note that the energy scales span different ranges in each panel. For more details, see the main text.

formed or spherical. The prolate local minimum becomes deeper with increasing N and for the nuclei $^{292,294}\text{Sg}$ an additional minimum is observed at the top of the second barrier. For $190 \leq N \leq 208$ the prolate local minimum further decreases its energy and becomes the ground state. The outer sectors of the fission paths exhibit a faster decline than the ones for Fm, No and Rf isotones. A fission barrier with a single hump determines the stability of the heaviest isotopes. Similar features have been found for Hs and Ds nuclei.

The HFB plus the zero point rotational energies, are depicted in Fig. 10 for $^{270-332}\text{Cn}$. The main features of the fission paths obtained for $^{270-290}\text{Cn}$ ($158 \leq N \leq 178$) are their prolate ground states and their wide two-humped barriers. For $180 \leq N \leq 192$, the ground states become weakly deformed or spherical. With increasing neutron number, the tendency found in lighter isotopes (i.e., the decrease in the height of the second hump of the original barrier) is reinforced due to the already very pronounced decline in the outer sectors of the fission paths. The inner barrier (i.e., the first hump of the original barrier) still plays a role though its height is severely reduced. A prolate well starts to develop after the inner barrier in the $N=190$ nucleus ^{302}Cn . With increasing

neutron number, this prolate well becomes deeper and the associated minimum turns out to be the ground state for $194 \leq N \leq 220$. Moreover, the outer sectors of the fission paths display a pronounced decline and a barrier with a single hump is obtained for the heaviest isotopes. A similar structural evolution has been obtained for the fission paths of the nuclei $^{274-338}\text{Fl}$ and $^{280-344}\text{Lv}$.

The HFB plus the zero point rotational energies are plotted in Fig. 11 for $^{288-348}\text{Og}$. For $^{288-296}\text{Og}$ ($170 \leq N \leq 178$) the ground states are prolate. Their fission barriers are wide with a prominent first hump followed, by a rather flat region. This flat region, further decreases its energy leading to a pronounced decline in the outer sectors of the fission paths obtained for $^{298-316}\text{Og}$ ($180 \leq N \leq 198$). The original hump reduces its height substantially and disappears with increasing N . For these nuclei, we also observe a pronounced reduction in the energy of the oblate configurations with increasing N . As a result, some of the fission paths exhibit a very complex topology characterized by a strong competition between oblate, spherical and prolate minima that makes the identification (oblate, spherical or prolate) of the actual ground state deformation in this kind of neutron-rich nuclei rather involved [49, 55, 104]. Obviously, what is

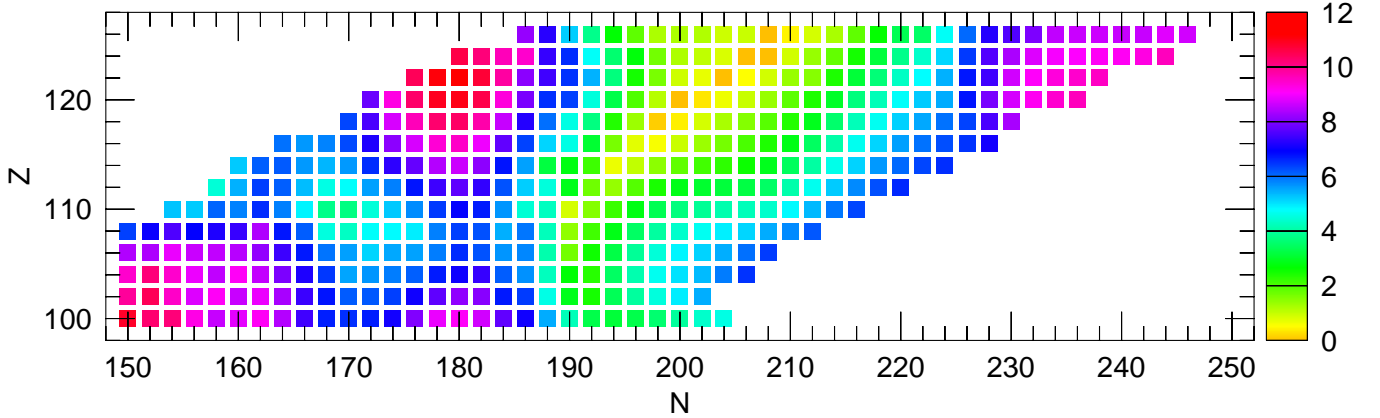


FIG. 12: (Color online) The height of the largest fission barrier for each nucleus is shown with a color code (on the right hand side, in MeV). Results have been obtained with the Gogny-D1M* EDF.

needed, in the presence of such a complex topology arising from multiple shape coexistent minima, is to account for quadrupole configuration mixing effects in the spirit of the GCM approach [39, 108, 109]. However, such a gigantic task is out of the scope of this study for several technical reasons (for example, the large number of HO shells used and the number of degrees of freedom required in the GCM ansatz).

For larger neutron numbers ($200 \leq N \leq 230$), the ground states are prolate in the case of $^{318-342}\text{Og}$ ($200 \leq N \leq 224$). The prolate wells ($Q_{20} \approx 20\text{b}$) become deeper while the fission barriers ($Q_{20} \approx 36\text{b}$) increase their heights. With increasing neutron number, however, we also observe the development of weakly deformed minima, around $Q_{20} = 0$. Those additional minima decrease their energies and already for ^{342}Og , we observe a very strong competition between them and the prolate ground state. This multipole shape coexistence also extends to the heaviest isotopes $^{344-348}\text{Og}$ whose ground states are predicted to be weakly oblate. For all these isotopes the energies of the fission paths decrease very quickly, as functions of the quadrupole moment, beyond the fission barriers. Similar comments do also apply for isotopic chains with larger Z values, i.e., $Z = 120, 122, 124$ and 126 .

As some of the fission barriers are rather low, we decided to check in those cases the effect of triaxial shapes in their heights. For this purpose we have carried out calculations in four representative nuclei, ^{300}Hs , ^{306}Cn , ^{314}Cn and ^{310}Fl . For those nuclei the axial barrier heights are 2.13, 1.42, 3.06 and 1.05 MeV, respectively. The inclusion of triaxial shapes lowers the barriers by 0.08, 0.06, 0 and 0.06 MeV, respectively. The maximum value of the triaxial deformation parameter γ never exceeds 5 degrees. Combining these results with those of Sec III A we observe a correlation between the height of the axial barrier and the amount of energy gained by allowing triaxial shapes: the largest the axial barrier height, the largest is the energy gain due to triaxial shapes. At least in the

examples studied the triaxial degree of freedom seems to play a minor role when the axial barrier heights are less than 3 or 4 MeV.

For each nucleus, the largest barrier height is plotted in Fig. 12 with a color code. The barriers are obtained without taking into account triaxial shapes and therefore the values given have to be considered as upper limits. Their evolution, as functions of the neutron number, provides a rough estimation of the stability of the considered nuclei against fission. As can be seen from the figure, our Gogny-D1M* calculations predict two regions of local maxima around ^{250}Fm and ^{300}Hs . Those regions are usually referred as the "peninsula of known nuclei" and the "island of stability", respectively. In our calculations, we have obtained barrier heights of up to 10.85 MeV for the former while for the latter the predicted heights reach up to 11.19 MeV. In between these two regions, the heights exhibit minima around $N = 168-170$ and decrease up to around 4 MeV. On the other hand, the lowest values of the barrier heights correspond to nuclei with neutron numbers $188 \leq N \leq 208$. In particular, vanishing barriers have been obtained for nuclei with the proton to neutron ratios $Z/N = 118/198, 118/200, 120/200, 122/202, 124/206, 124/208$ and $126/208$. Regions of vanishing barriers have already been predicted within the Mac-Mic and mean-field approaches [27, 55, 62, 113]. They play an important role to determine the Z/N ratios around which the r-process nucleosynthesis of superheavy elements is terminated by neutron induced fission [114, 115]. Beyond those regions of vanishing barriers, the heights increase as functions of N for all the considered isotopic chains. Qualitatively, our results compare well with the ones obtained in previous studies [27, 55, 62, 113] though quantitative differences are observed, especially for neutron-rich nuclei. However, calculations of fission reaction rates are required to better understand the sensitivity of the r-process abundances with respect to the fission properties predicted within different theoretical models.

The spontaneous fission half-lives t_{SF} , predicted within

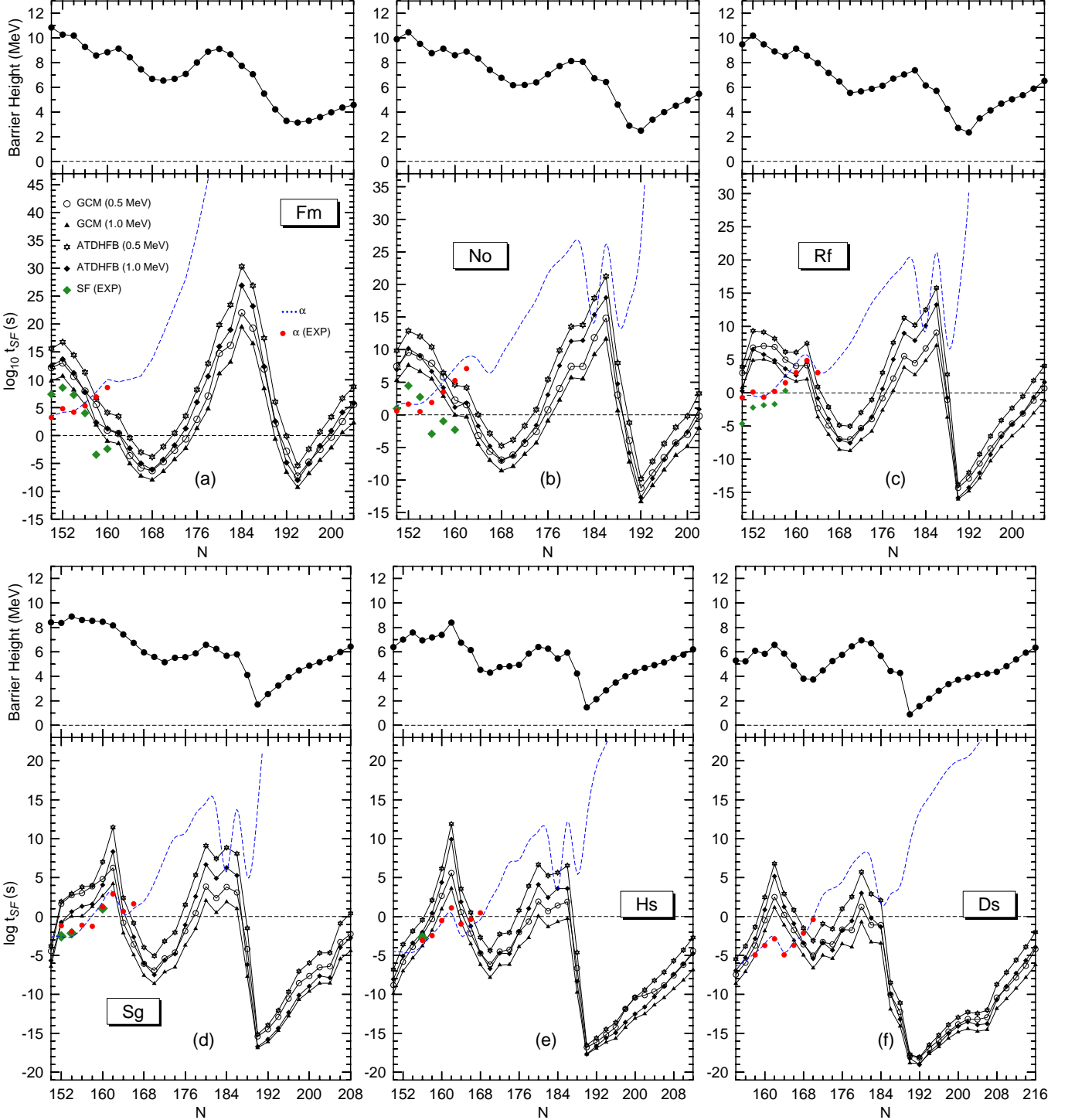


FIG. 13: (Color online) The spontaneous fission half-lives t_{SF} , predicted within the GCM and ATDHFB schemes for the collective inertias, are shown for the Fm, No, Rf, Sg, Hs and Ds isotopic chains as functions of the neutron number in panels (a) to (f). Results have been obtained with the Gogny-D1M* EDF. Calculations have been carried out with $E_0 = 0.5$ MeV and $E_0 = 1.0$ MeV. The experimental t_{SF} values [86, 87] are included in the plots as green diamonds. The α -decay half-lives are plotted with short dashed lines in each panel. Experimental values (red dots) have been taken from Ref. [110]. In addition, the largest fission barrier heights are plotted at the top of each panel. For more details, see the main text.

the GCM and ATDHFB schemes for the collective inertias, are shown in panels (a) to (f) of Fig. 13 for the Fm, No, Rf, Sg, Hs and Ds isotopic chains as functions of the neutron number. The corresponding results for the Cn, Fl, Lv, Og, $Z = 120$ and $Z = 122$ chains are shown in Fig. 14 and the ones for nuclei with $Z = 124$ and $Z = 126$ in Fig. 15. The largest barrier height (see, Fig. 12) is plotted at the top of each panel for each isotope.

Before discussing the t_{SF} values let us mention an assumption made to deal with those nuclei with an oblate ground state. In this case, the nucleus can proceed to fission by climbing the spherical maximum or it can take a detour through the γ plane (see [116] for a recent example). As the energy of the oblate minimum is, in most of the cases, rather close to the one of the prolate configuration we are in the typical case of shape coexistence. In those cases, the oblate and prolate minima have roughly the same absolute value of β_2 and are connected through an arc in the γ plane. As a systematic calculation of tri-axial configurations is prohibitive for the large configuration spaces used, we have assumed that the contribution to the action (entering the WKB formula) from the tri-axial path connecting the oblate and prolate minimum or from the the axially symmetric path going through the spherical maximum can be neglected. This assumption is justified by the expected very small energy barrier between the oblate and prolate minima that lead to a negligible contribution to the action, as compared to the one corresponding to the path going from the prolate minimum to scission through the first fission barrier, as this barrier is usually far much larger [117] (see, for instance, the case of ^{300}Og and neighboring nuclei, in Fig. 11).

Regardless of the E_0 value and/or the scheme employed, the trend in the predicted spontaneous fission half-lives resembles, as expected, the one obtained for the barrier heights. Nevertheless, for a given nucleus, the probability to penetrate the fission barrier depends on several other ingredients and cannot be solely determined by the barrier height. In particular, one should keep in mind that the predicted t_{SF} values are also affected, for example, by the barrier shapes (mainly their width) and the behavior and size of the collective inertia. Therefore, calculations involving the latter should be carried out to make quantitative predictions.

For all the studied isotopic chains, the spontaneous fission half-lives display maxima around $N = 180$ -186, that reflect the effect of the $N = 184$ neutron shell closure. Immediately after those maxima there is a sudden dip around $N = 188$ -194 for $100 \leq Z \leq 118$ and around $N = 200$ for $120 \leq Z \leq 126$ with very small values of t_{SF} . Those very small values (up to $t_{SF} \approx 10^{-21}$ s) correspond to nuclei with very small and/or vanishing barrier heights. The subsequent increase observed in the t_{SF} values for larger neutron numbers correlates well with the increase observed in the heights of the (prolate) barriers that emerge in the fission paths of the heaviest nuclei in each isotopic chain (see, Figs. 8, 9, 10, 11). For Fm, No and Rf nuclei, our calculations predict local maxima at

$N = 152$ that reflect shell effects arising from the corresponding gap in the neutron single-particle spectrum [see, panel (a) of Fig. 4]. In the case of Fm and No isotopes, a small kink is observed around $N = 162$ whereas for Rf nuclei the effect of this deformed shell closure on the lifetimes is more pronounced. On the other hand, for $106 \leq Z \leq 114$ the first local maximum is located at $N = 162$. Note that, with increasing Z values, we observe a shape change in the fission barriers around $N = 162$. First, for low Z values a single barrier is obtained around $N = 162$. Then, the barrier becomes wider and two-humped. However, further increasing Z we observe a severe reduction in the height of the second hump together with a pronounced decline in the outer sections of the fission paths. This leads to much smaller t_{SF} values for Fl isotopes around $N = 162$ as compared with, for example, the ones obtained for Cn isotopes around the same neutron number. In our Gogny-D1M* calculations, both the barrier heights and the spontaneous fission half-lives exhibit a local minimum around $N = 168$ -170 which also correlates well with the structural evolution observed in the fission paths around these neutron numbers.

Although the previous discussion shows that the trend with neutron number of t_{SF} is rather insensitive to the details, like the E_0 value used or the scheme adopted for the calculation of the collective inertias, the specific values of t_{SF} really depend on them. For instance, the lifetimes obtained with the ATDHFB inertias tend to be larger than the ones obtained in the GCM framework for a given E_0 . The difference becomes more pronounced the higher and wider the fission barriers are as can be observed in previous calculations for neutron-rich Ra, U and Pu nuclei [17-19]. For example, we have obtained for the lighter Fm isotopes $^{250-254}\text{Fm}$, with $E_0 = 0.5$ MeV, the values $\log_{10} t_{SF}^{GCM} = 12.19, 13.03, 10.62$ and $\log_{10} t_{SF}^{ATDHFB} = 15.60, 16.77, 14.44$. The comparison with the available experimental t_{SF} values [86, 87] reveals that our results overestimate them though the trend with neutron number is reproduced reasonably well in most of the cases. Larger E_0 values are required to improve the agreement with the experiment. For example, for $^{250-254}\text{Fm}$ [see, panel (a) of Fig. 13], with $E_0 = 1.0$ MeV, we have obtained $\log_{10} t_{SF}^{GCM} = 9.81, 10.65, 8.18$ and $\log_{10} t_{SF}^{ATDHFB} = 12.47, 13.68, 11.22$.

In Figs. 13, 14 and 15, we have also plotted the α -decay half-lives computed with a parametrization [16] of the Viola-Seaborg formula [15] Eq. (5). The predicted α -decay lifetimes agree well with the available experimental data [110]. A comparison of the Q_α values obtained in our Gogny-D1M* calculations with the available experimental data yields the rms value $\sigma(Q_\alpha) = 0.27$ MeV. The same comparison for $\log_{10} t_\alpha$ yields $\sigma(\log_{10} t_\alpha) = 0.84$. On the one hand, α -decay mainly dominates in the proton-rich regions. On the other hand, fission turns out to be faster than α -decay with increasing neutron number. In Fig. 16, we have plotted the logarithm of the shortest half-life (in seconds) for the studied nuclei. In spite of the quantitative differences, the patterns emerg-

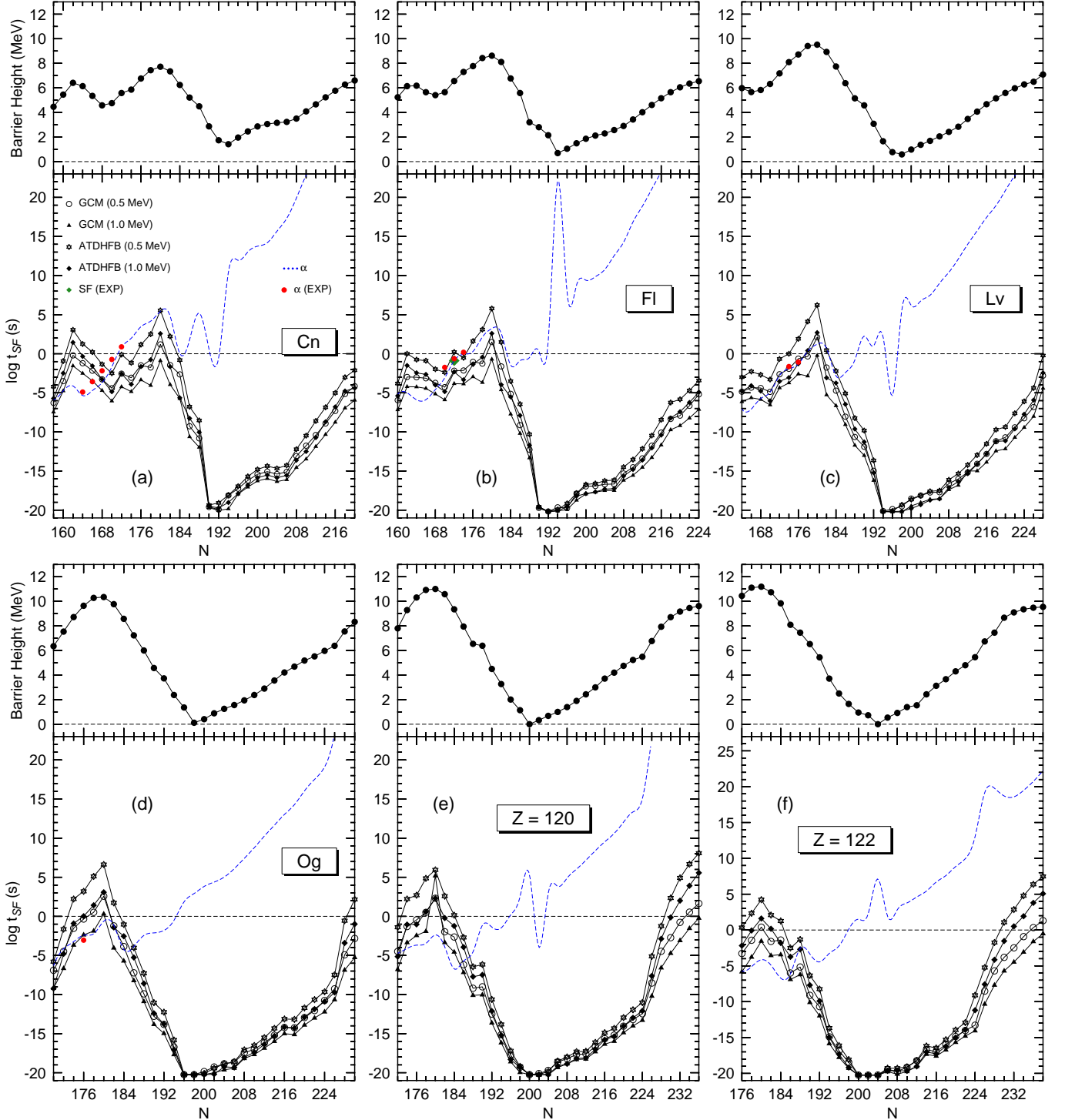


FIG. 14: (Color online) The same as Fig. 13 but for the Cn, Fl, Lv, Og, $Z = 120$ and $Z = 122$ isotopic chains.

ing within the GCM [panel (a)] and ATDHFB [panel (b)] schemes for the collective inertias, with $E_0 = 1.0$ MeV, are very similar. The same is also true for $E_0 = 0.5$ MeV and, therefore, they are not shown in the figure. Typically, experimental techniques allow the full characterization of nuclei with half-lives larger than $10 \mu\text{s}$. In

our calculations, long living nuclei are predicted around $Z = 106$ and $N = 160$. For example, for ^{266}Sg we have obtained half-lives around 10^2 s. A second region of long living nuclei is predicted around $N = 180$. For example, for the $N = 180$ isotones ^{288}Hs , ^{290}Ds , ^{292}Cn and ^{294}Fl , for which fission is the dominant decay mode, we have ob-

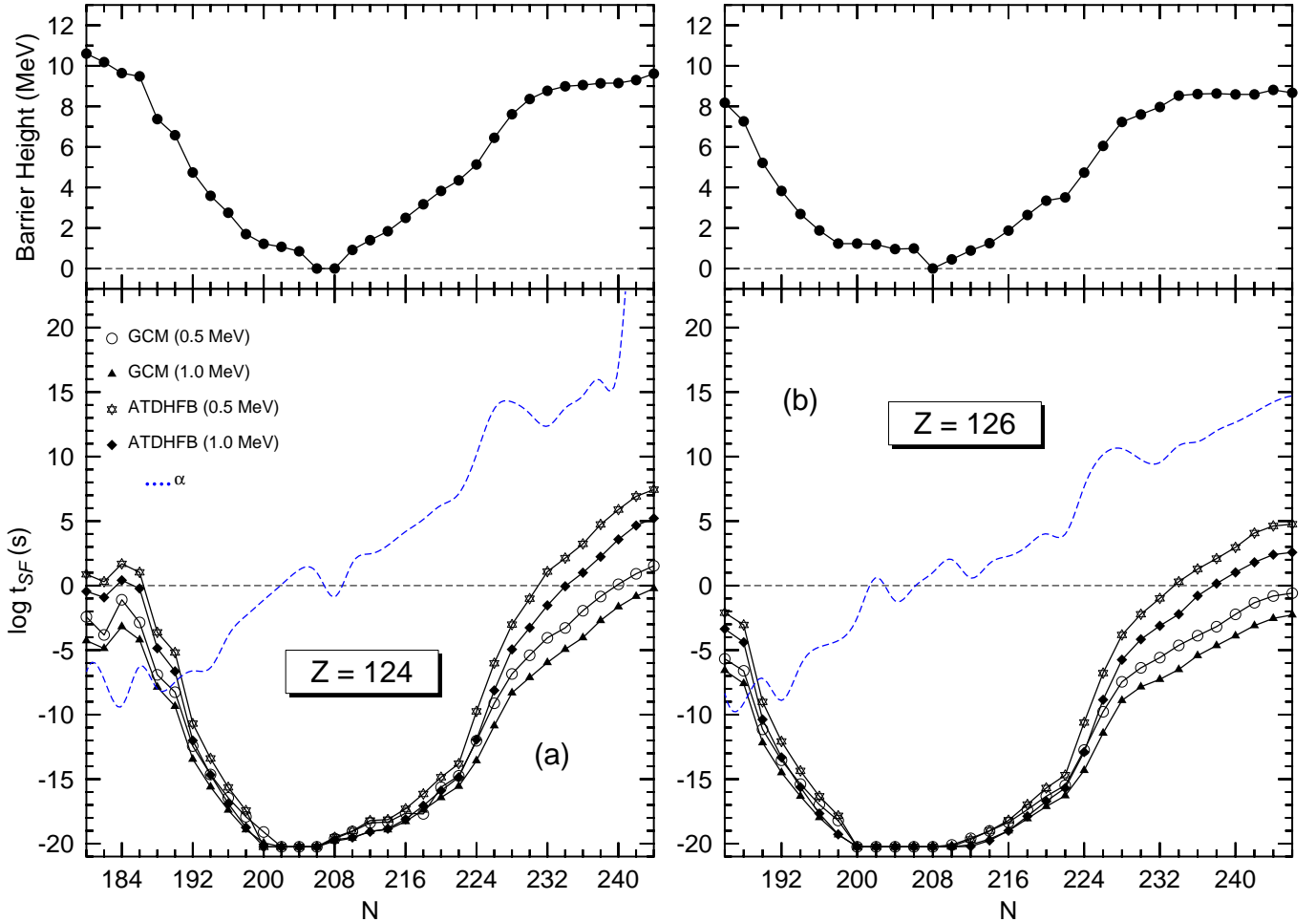


FIG. 15: (Color online) The same as Fig. 13 but for $Z = 124$ and $Z = 126$ isotopic chains.

tained $t_{SF}^{GCM} = 1.16, 0.19, 0.13$ and 0.20 s while $t_{SF}^{ATDHFB} \approx 10^4$ s for ^{288}Hs and $t_{SF}^{ATDHFB} \approx 10^3$ s for ^{290}Ds , ^{292}Cn and ^{294}Fl , respectively. For larger neutron numbers, we have obtained a region centered around $Z = 120$ and $N = 204$ for which the half-lives are too short to be characterized experimentally. Finally, the increase observed in the fission barriers obtained for the most neutron-rich isotopes in each of the studied chains leads to larger half-lives. We find, that the overall pattern emerging from Fig. 16 agrees well with the ones obtained in previous studies [49, 55].

IV. SUMMARY AND CONCLUSIONS

In this work, the constrained HFB approximation, based on the new parametrization D1M* of the Gogny-EDF, is used to study the properties of 435 even-even superheavy elements. Besides the usual constraints on both the proton \hat{Z} and neutron \hat{N} number operators, we have considered constraints on the quadrupole \hat{Q}_{20} and octupole \hat{Q}_{30} as well as on the \hat{Q}_{10} operators. Due to

the very time demanding nature of the calculations, axial symmetry has been kept as a selfconsistent symmetry. A large and optimized (deformed) axially symmetric HO basis has been employed. Zero-point quantum corrections have always been added to the HFB energies *a posteriori*. In particular, the rotational energy correction has been computed in terms of the Yoccoz moment of inertia while the GCM and ATDHFB schemes have been used to compute both the collective masses and vibrational energy corrections. Having extracted all the required building blocks from the mean-field calculations, we have computed the spontaneous fission half-lives t_{SF} within the WKB formalism. The α -decay half-lives have been obtained with a parametrization of the Viola-Seaborg formula.

The newly proposed D1M* parametrization is based on the previous D1M parametrization of the Gogny force and it imposes a more realistic value of the slope L of the symmetry energy. As a consequence, the properties of very neutron-rich nuclei are expected to differ from those of D1M and to be more accurate in the description of nuclei with strong proton-neutron asymmetry. Neutron

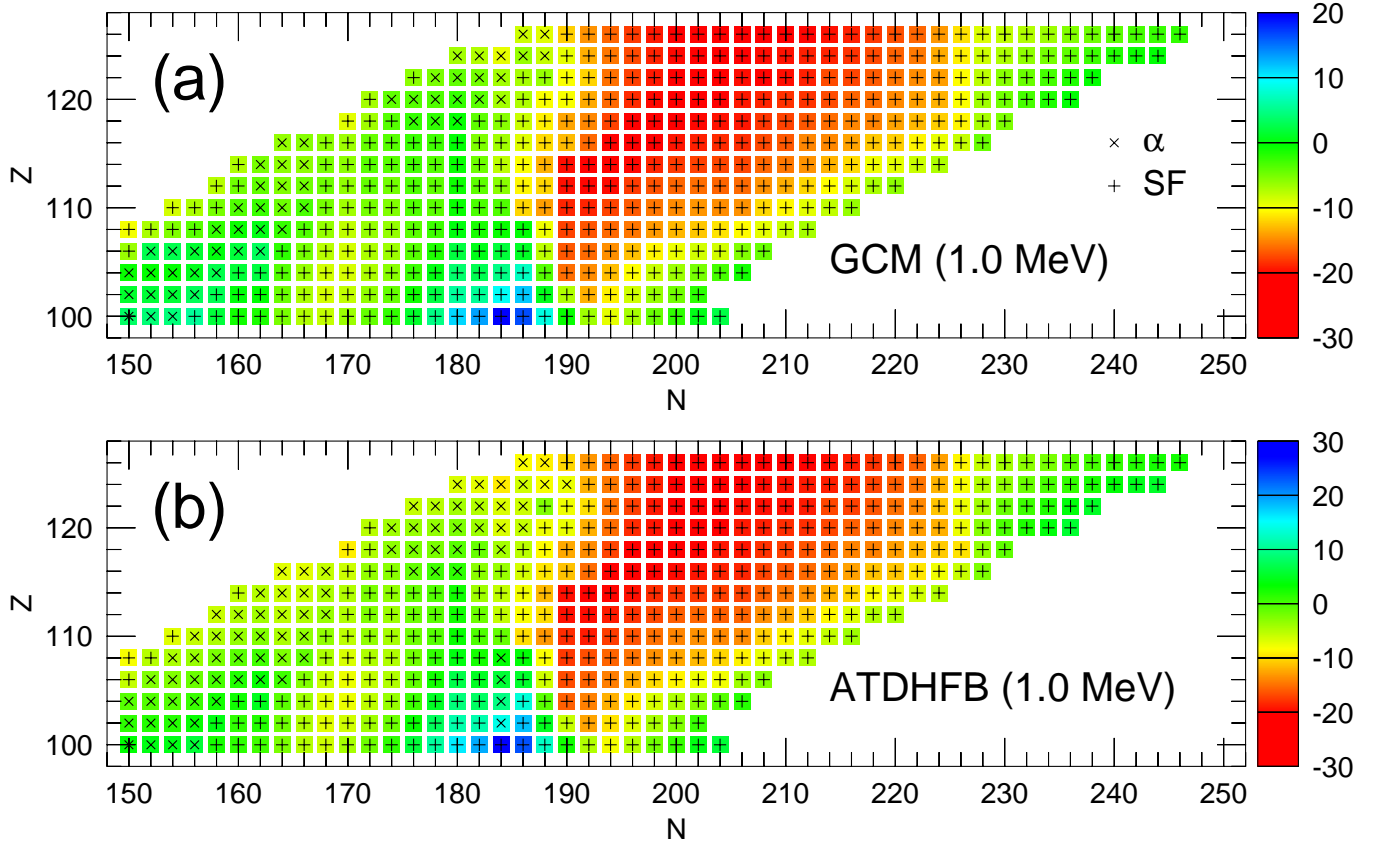


FIG. 16: (Color online) Logarithm of the shortest (spontaneous fission or α -decay) half-life (in seconds) obtained for the nuclei studied in this work within the GCM [panel (a)] and ATDHFB [panels (b)] collective inertia schemes. Results correspond to the Gogny-D1M* EDF and $E_0 = 1.0$ MeV. For more details, see the main text.

rich nuclei are specially relevant for the description of the nucleo-synthesis mechanism.

The parametrization D1M* has been benchmarked against available experimental data on inner and second barrier heights, excitation energies of fission isomers and spontaneous fission half-lives in a selected set of Pu, Cm, Cf, Fm, No, Rf, Sg, Hs and Fl nuclei. It is shown that the global trends observed in the experiment are reproduced reasonably well. The second barrier heights come up a bit too high (2-4 MeV), a discrepancy that is not expected to be reduced by including triaxial shapes. This disagreement with the experimental data remains to be analyzed in detail.

We have described the methodology employed to obtain the fission paths of the studied nuclei and paid special attention to proton and neutron pairing correlations, octupole and hexadecupole deformations as well as collective GCM and ATDHFB masses. Energy gaps in the proton and neutron single-particle spectra have been analyzed. From the comparison with the available experimental data and the results obtained in previous studies, especially in the case of the Gogny-D1M EDF, we concluded that D1M* represents a reasonable starting point to describe fission in heavy and superheavy nuclei.

We have performed a detailed study of the (minimal energy) fission paths in superheavy nuclei. First, we have considered the systematic of the ground state quadrupole β_2 and octupole β_3 deformation parameters. Octupole deformed ground states have been predicted for nuclei with neutron numbers $186 \leq N \leq 194$. Ground state proton and neutron pairing energies as well as two-nucleon separation energies have been thoroughly discussed. The latter compare well with the available experimental data and with results obtained with the Gogny-D1M EDF.

A detailed discussion of the structural changes observed in the fission paths of the considered nuclei has been carried out as a function of both Z and N . The (largest) barrier heights resulting from those structural changes exhibit local maxima in the "peninsula of known nuclei" (i.e., around $Z = 100$ and $N = 150$) and the "island of stability" (i.e., around $Z = 120$ and $N = 180$) whereas local minima are found for nuclei with $N = 168-170$. Moreover, small and/or vanishing barrier heights have been obtained for $188 \leq N \leq 208$ followed by a region of increasing barrier heights for all the studied isotopic chains. Qualitatively, our results compare well with the ones obtained in previous studies though quantitative differences are observed, especially for neutron-rich

nuclei.

The GCM and/or ATDHFB spontaneous fission half-lives, computed with $E_0 = 0.5$ MeV and $E_0 = 1.0$ MeV, exhibit a trend with neutron number that resembles the one obtained for the largest of the barrier heights in each isotope. However, effects associated, for example, with the shape and width of the fission barriers, shell closures as well as the collective masses also play a role to determine local variations in the stability against spontaneous fission. The predicted t_{SF} values overestimate the experimental ones though the trend with neutron number is reproduced reasonably well. On the other hand, the α -decay half-lives obtained in our calculations agree well with the available experimental data. The α -decay mainly dominates in the proton-rich regions of the superheavy landscape while, with increasing neutron number, fission becomes faster. Long living nuclei, with half-lives greater than $10 \mu s$, have been found around $Z = 106$ and $N = 160$ and around the neutron number $N = 180$. On the other hand, the half-lives for nuclei around $Z = 120$ and $N = 204$ are too short to be characterized experimentally. Larger half-lives, associated with the increase in the corresponding barrier heights, have been obtained for the most neutron-rich isotopes in each of the studied isotopic chains. This overall pattern, also agrees well with the ones obtained in previous studies.

A long list of tasks remains to be undertaken in future studies. For example, consider triaxial deformation in all the stages of the calculation to justify or discredit the general arguments used to skip its impact on the eval-

uation of t_{SF} . Calculations for odd-even and odd-odd superheavy nuclei should be carried out in order to further assess the predictive power of the Gogny-D1M* EDF. Given the technical difficulties associated with those calculations, the Equal Filling Approximation (EFA) appears as a plausible (selfconsistent) candidate for such studies [20, 21]. Moreover, it has been recently shown [24] that for Fm and No nuclei the inclusion of pairing fluctuations, associated with the spontaneously broken U(1) particle number symmetry, within a least action approach improves the agreement between the predicted t_{SF} values and the experiment. Within such an approach [23, 24], a minimization of the action is carried out, with respect to some parameter correlated with the amount of pairing correlations, for each of the configurations along the minimal energy fission path of a given nucleus. Therefore, the (minimal energy) fission paths computed in this work might represent the basis for the corresponding large scale least action calculations. Work along these lines is in progress and will be reported elsewhere.

Acknowledgments

The work of LMR was partly supported by the Spanish MINECO Grant No. FPA2015-65929, No. FIS2015-63770 and No. PGC2018-094583-B-I00.

[1] H.J. Specht, Rev. Mod. Phys. **46**, 773 (1974).

[2] S. Björnholm and J.E. Lynn, Rev. Mod. Phys. **52**, 725 (1980).

[3] L. Meitner and O.R. Frisch, Nature **143**, 239 (1939).

[4] N. Bohr and J.A. Wheeler, Phys. Rev. **56**, 426 (1939).

[5] M. Brack, J. Damgaard, A.S. Jensen, H.C. Pauli, V.M. Strutinsky and C.Y. Wong, Rev. Mod. Phys. **44**, 320 (1972).

[6] A. Baran, M. Kowal, P. -G. Reinhard, L. M. Robledo, A. Staszczak and M. Warda, Nucl. Phys. A **994**, 442 (2015).

[7] N. Schunck and L. M. Robledo, Rep. Prog. Phys. **79**, 116301 (2016).

[8] W. Nazarewicz, Nature Physics **14**, 537 (2018).

[9] S. Goriely, Eur. Phys. J. A **51**, 22 (2015).

[10] J. J. Cowan, F. -K. Thielemann and J. W. Truran, Phys. Rep. **208**, 267 (1991).

[11] G. Martínez-Pinedo, D. Mocelj, N. M. Zinner, A. Kelić-Heil, K. Langanke, I. V. Panov, B. Pfeiffer, T. Rauscher, K. -H. Schmidt and F. -K. Thielemann, Prog. Part. Nucl. Phys. **59**, 199 (2007).

[12] S. Goriely, J. -L. Sida, J. -F. Lemaitre, S. Panebianco, N. Dubray, S. Hilaire, A. Bauswein and H. -T. Janka, Phys. Rev. Lett. **111**, 242502 (2013).

[13] M. Eichler, A. Arcones, A. Kelic, O. Korobin, K. Langanke, T. Marketin, G. Martínez-Pinedo, I. Panov, T. Rauscher, S. Rosswog, C. Winteler, N. T. Zinner and F. -K. Thielemann, Astrophys. J. **808**, 30 (2015).

[14] J. J. Mendoza-Temis, M. -R. Wu, K. Langanke, G. Martínez-Pinedo, A. Bauswein and H. -T. Janka, Phys. Rev. C **92**, 055805 (2015).

[15] V.E. Viola Jr. and G.T. Seaborg, J. Inorg. Nucl. Chem. **28**, 741 (1966).

[16] T. Dong and Z. Ren, Eur. Phys. J. A **26**, 69 (2005).

[17] R. Rodríguez-Guzmán and L. M. Robledo, Phys. Rev. C **89**, 054310 (2014).

[18] R. Rodríguez-Guzmán and L. M. Robledo, Eur. Phys. J. A **50**, 142 (2014).

[19] R. Rodríguez-Guzmán and L. M. Robledo, Eur. Phys. J. A **52**, 12 (2016).

[20] R. Rodríguez-Guzmán and L. M. Robledo, Eur. Phys. J. A **52**, 348 (2016).

[21] R. Rodríguez-Guzmán and L. M. Robledo, Eur. Phys. J. A **53**, 245 (2017).

[22] S.A. Giuliani and L.M. Robledo, Phys. Rev. C **88**, 054325 (2013).

[23] S.A. Giuliani, L. M. Robledo and R. Rodríguez-Guzmán, Phys. Rev. C **90**, 054311 (2014).

[24] R. Rodríguez-Guzmán and L. M. Robledo, Phys. Rev. C **98**, 034308 (2018).

[25] H.J. Krappe and K. Pomorski, *Theory of Nuclear Fission*, Lectures Notes in Physics, **838** (Springer, Berlin,

2012).

[26] C. Wagemans, *The Nuclear Fission Process* (CRC Press, Boca Raton, 1991).

[27] P. Möller, A. J. Sierk, T. Ichikawa, A. Iwamoto and M. Mumpower, Phys. Rev. C **91**, 024310 (2015).

[28] R. Julin, Nucl. Phys. A **834**, 15c (2010).

[29] Yu.Ts. Oganessian, F.Sh. Abdullin, S.N. Dmitriev, J.M. Gostic, J.H. Hamilton, R.A. Henderson, M. G. Itkis, K.J. Moody, A.N. Polyakov, A.V. Ramayya, J.B. Roberto, K.P. Rykaczewski, R.N. Sagaidak, D.A. Shaughnessy, I.V. Shirokovsky, M.A. Stoyer, V.G. Subbotin, A.M. Sukhov, Yu.S. Tsyanov, V.K. Utyonkov, A.A. Voinov and G.K. Vostokin, Phys. Rev. Lett. **108**, 022502 (2012).

[30] H. Haba, D. Kaji, H. Kikunaga, Y. Kudou, K. Morimoto, K. Morita, K. Ozeki, T. Sumita, A. Yoneda, Y. Kasamatsu, Y. Komori, K. Ooe and A. Shinohara, Phys. Rev. C **83**, 034602 (2011).

[31] V.M. Strutinsky, Nucl. Phys. A **95**, 420 (1967).

[32] V.M. Strutinsky, Nucl. Phys. A **122**, 1 (1968).

[33] W.D. Myers and W.J. Swiatecki, Nucl. Phys. A **81**, 1 (1966).

[34] P. Möller and A. Iwamoto, Phys. Rev. C **61**, 047602 (2000).

[35] P. Möller, D.G. Madlan, A.J. Sierk and A. Iwamoto, Nature **409**, 785 (2001).

[36] Z. Patyk and A. Sobczewski, Phys. Lett. B **256**, 307 (1991); Nucl. Phys. A **533**, 132 (1991).

[37] P. Jachimowicz, M. Kowal and J. Skalski, Phys. Rev. C **92**, 044306 (2015).

[38] P. Jachimowicz, M. Kowal and J. Skalski, Phys. Rev. C **95**, 014303 (2017).

[39] P. Ring and P. Schuck, *The Nuclear Many-Body Problem* (Springer, Berlin, 1980).

[40] J. F. Berger, M. Girod, and D. Gogny, Nucl. Phys. A **428**, 23c (1984).

[41] J.-F. Berger, L. Bitaud, J. Decharge, M. Girod and K. Dietrich, Nucl. Phys. A **685**, 1c (2001).

[42] J.-P. Delaroche, M. Girod, H. Goutte and J. Libert, Nucl. Phys. A **771**, 103 (2006).

[43] V. Martin and L.M. Robledo, Int. J. Mod. Phys. E **18**, 788 (2009).

[44] N. Dubray, H. Goutte and J.-P. Delaroche, Phys. Rev. C **77**, 014310 (2008).

[45] S. Pérez-Martín and L.M. Robledo, Int. J. Mod. Phys. E **18**, 861 (2009).

[46] W. Younes and D. Gogny, Phys. Rev. C **80**, 054313 (2009).

[47] M. Warda, J. L. Egido, L.M. Robledo and K. Pomorski, Phys. Rev. C **66**, 014310 (2002).

[48] J.L. Egido and L.M. Robledo, Phys. Rev. Lett. **85**, 1198 (2000).

[49] M. Warda and J.L. Egido, Phys. Rev. C **86**, 014322 (2012).

[50] N. Nikolov, N. Schunck, W. Nazarewicz, M. Bender and J. Pei, Phys. Rev. C **83**, 034305 (2011).

[51] J.D. McDonnell, W. Nazarewicz and J.A. Sheikh, Phys. Rev. C **87**, 054327 (2013).

[52] J. Erler, K. Langanke, H.P. Loens, G. Martínez-Pinedo and P.-G. Reinhard, Phys. Rev. C **85**, 025802 (2012).

[53] A. Staszczak, A. Baran, W. Nazarewicz, Physical Review C **87**, 024320 (2013).

[54] A. Baran, K. Pomorski, A. Lukasiak and A. Sobczewski, Nucl. Phys. A **361**, 83 (1981).

[55] S. Giuliani, G. Martínez-Pinedo and L. M. Robledo, Phys. Rev. C **97**, 034323 (2018).

[56] M. Bender, K. Rutz, P.-G. Reinhard, J.A. Maruhn and W. Greiner, Phys. Rev. C **58**, 2126 (1998).

[57] H. Abusara, A.V. Afanasjev and P. Ring, Phys. Rev. C **82**, 044303 (2010).

[58] H. Abusara, A.V. Afanasjev and P. Ring, Phys. Rev. C **85**, 024314 (2012).

[59] B.-N. Lu, E.-G. Zhao and S.-G. Zhou, Phys. Rev. C **85**, 011301 (2012).

[60] S. Karatzikos, A. V. Afanasjev, G. A. Lalazissis and P. Ring, Phys. Lett. B **689**, 72 (2010).

[61] S. E. Agbemava, A. V. Afanasjev, A. Taninah and A. Gyawali, Phys. Rev. C **99**, 034316 (2019).

[62] S. E. Agbemava, A. V. Afanasjev and P. Ring, Phys. Rev. C **95**, 054324 (2017).

[63] L.M. Robledo, T. R. Rodríguez and R. Rodríguez-Guzman, J. Phys. G: Nucl. Part. Phys. **46**, 013001 (2019).

[64] B. Friedman and V. R. Pandharipande, Nucl. Phys. A **361**, 502 (1981).

[65] F. Chappert, M. Girod, and S. Hilaire, Phys. Lett. B **668**, 420 (2008).

[66] R. Rodríguez-Guzmán, L.M. Robledo, P. Sarriguren and J. E. García-Ramos, Phys. Rev. C **81**, 024310 (2010).

[67] L.M. Robledo and R. Rodríguez-Guzmán, J. Phys. G: Nucl. Part. Phys. **39**, 105103 (2012).

[68] L.M. Robledo and G. F. Berstch, Phys. Rev. C **84**, 054302 (2011).

[69] L. M. Robledo, J. Phys. G: Nucl. Part. Phys. **42**, 055109 (2015)

[70] S. Goriely, S. Hilaire, M. Girod and S. Péru, Phys. Rev. Lett. **102**, 242501 (2009).

[71] R. Rodríguez-Guzmán, L.M. Robledo and P. Sarriguren, Phys. Rev. C **86**, 034336 (2012).

[72] R. Rodríguez-Guzmán, P. Sarriguren, L.M. Robledo, and S. Perez-Martin, Phys. Lett. B **691**, 202 (2010).

[73] L.M. Robledo, R. Rodríguez-Guzmán, and P. Sarriguren, J. Phys. G: Nucl. Part. Phys. **36**, 115104 (2009).

[74] R. Rodríguez-Guzmán, P. Sarriguren, and L.M. Robledo, Phys. Rev. C **82**, 061302(R) (2010).

[75] R. Rodríguez-Guzmán, P. Sarriguren, and L.M. Robledo, Phys. Rev. C **83**, 044307 (2011).

[76] D. T. Loan, N. H. Tan, D. T. Khoa and J. Margueron, Phys. Rev. C **83**, 065809 (2011).

[77] R. Sellahewa and A. Rios, Phys. Rev. C **90**, 054327 (2014).

[78] C. Gonzalez-Boquera, M. Centelles, X. Vinas and A. Rios, Phys. Rev. C **96**, 065806 (2017).

[79] P. B. Demorest, T. Pennucci, S. M. Ransom, M. S. E. Roberts and J. W. T. Hessels, Nature **467**, 1081 (2010).

[80] J. Antoniadis *et al.*, Science **340**, 448 (2013).

[81] C. Gonzalez-Boquera, M. Centelles, X. Vinas and L. M. Robledo, Phys. Lett. B **779**, 195 (2018)

[82] C. Gonzalez-Boquera, M. Centelles, X. Vinas and L. M. Robledo, in preparation.

[83] S. Goriely and G. Martínez-Pinedo, Nucl. Phys. A **944**, 158 (2015).

[84] B. Singh, R. Zywina and R. Firestone, Nucl. Data Sheets **97**, 241 (2002).

[85] R. Capote *et al.*, Nucl. Data Sheets **110**, 3107 (2009).

[86] N.E. Holden and D.C. Hoffman, Pure Appl. Chem. **72**, 1525 (2000).

[87] G F Bertsch and W Loveland and W Nazarewicz and P

Talou, J. Phys. G**42**, 077001 (2015).

[88] L. M. Robledo and G. F. Berstch, Phys. Rev. C **84**, 014312 (2011).

[89] C. Titin-Schnaider and Ph. Quentin, Phys. Lett. B **49**, 213 (1974).

[90] Z. Shi, A. V. Afanasjev, Z. P. Li and J. Meng, Phys. Rev. C **99**, 064316 (2019).

[91] M. Girod and B. Grammaticos, Nucl. Phys. A **330**, 40 (1979).

[92] M.J. Giannoni and P. Quentin, Phys. Rev. C **21**, 2060 (1980); Phys. Rev. C **21**, 2076 (1980).

[93] J. Libert, M. Girod and J.P. Delaroche, Phys. Rev. C **60**, 054301 (1999).

[94] R. Rodríguez-Guzmán, J.L. Egido and L.M. Robledo, Phys. Lett. B **474**, 15 (2000); Phys. Rev. C **62**, 054308 (2000).

[95] J.L. Egido and L.M. Robledo, Lectures Notes in Physics **641**, 269 (2004).

[96] J. Zhao, B. -N. Lu, T. Niksic, D. Vretenar and S. -G. Zhou, Phys. Rev. C **93**, 044315 (2016).

[97] J. Sadhukhan, J. Dobaczewski, W. Nazarewicz, J. A. Sheikh, and A. Baran, Phys. Rev. C **90**, 061304(R) (2014).

[98] J. Sadhukhan, W. Nazarewicz and N. Schunck, Phys. Rev. C **93**, 011304 (2016).

[99] M. Martini, A. de Pace, and K. Bennaceur, Eur. Phys. J. A **55**, 250 (2019)

[100] C. Gonzalez-Boquera, M. Centelles, X. Vias, L. M. Robledo, arXiv:1807.10159

[101] C. Gonzalez-Boquera, M. Centelles, X. Vias, L. M. Robledo, to be submitted

[102] S. E. Agbemava, A. V. Afanasjev, T. Nakatsukasa and P. Ring, Phys. Rev. C **92**, 054310 (2015).

[103] M. Bender and P. -H. Heenen, J. Phys. Conf. Series **420**, 012002 (2013).

[104] <http://www-phynu.cea.fr/HFB-Gognyeng.htm>.

[105] P. Möller, J. R. Nix, W. D. Myers and W.J. Swiatecki, At. Data and Nucl. Data Tables **59**, 185 (1995).

[106] S. E. Agbemava and A. V. Afanasjev, Phys. Rev. C **96**, 024301 (2017).

[107] I. Muntian, S. Hofmann, Z. Patyk and A. Sobiczewski, Acta Phys. Pol. B **668**, 420424 (2003).

[108] R. Rodríguez-Guzmán, L. M. Robledo and M. M. Sharma, Eur. Phys. J. A **51**, 73 (2015).

[109] M. Bender, G. F. Bertsch and P. -H. Heenen, Phys. Rev. C **73**, 034322 (2006).

[110] Meng Wang, G. Audi, F. G. Kondev, W. J. Huang, S. Naimi and Xing Xu, Chinese Phys. C **41**, 030003 (2017).

[111] R. Rodríguez-Guzmán, J.L. Egido and L.M. Robledo, Phys. Rev. C **69**, 054319 (2004).

[112] R. Rodríguez-Guzmán, J.L. Egido, and L.M. Robledo, Nucl. Phys. A **709**, 201 (2002).

[113] S. Goriely, S. Hilaire, A. J. Koning, M. Sin and R. Capote, Phys. Rev. C **79**, 024612 (2009).

[114] I. V. Panov, I. Y. Korneev, T. Rauscher, G. Martínez-Pinedo, A. Kelia-Heil, N. T. Zinner and F. -K. Thielemann, Astron. Astrophysics **513**, A61 (2010).

[115] I. Petermann, K. Langanke, G. Martínez-Pinedo, I. V. Panov, P. -G. Reinhard and F. -K. Thielemann, Eur. Phys. J. A **48**, 122 (2012).

[116] W. Ryssens, M. Bender, K. Bennaceur, P.-H. Heenen, and J. Meyer, Phys. Rev. C **99**, 044315 (2019)

[117] S. Cwiok, P. -H. Heenen and W. Nazarewicz, Nature **433**, 705 (2005).